Mixing of strongly diffusive passive scalars like temperature by turbulence

By CARL H. GIBSON†, WILLIAM T. ASHURST‡
AND ALAN R. KERSTEIN‡

† University of California at San Diego, La Jolla, CA 92093, USA

‡ Thermofluids Division, Sandia National Laboratories, Livermore, CA 94550, USA

Mechanisms of turbulent mixing are explored by numerical simulations of one-dimensional and two-dimensional mixing with $Pr < 1$. The simulations suggest that the local rate of strain γ mixes the scalar field by at least two interacting mechanisms: the mechanism of generation, pinching and splitting of extrema proposed by Gibson (1968a) which acts along lines where the scalar-gradient magnitude is small; and a new mechanism of alignment, pinching and amplification of the gradients which acts along lines where the scalar-gradient magnitude is large. After extrema are generated, they split to form new extrema of the same sign, and saddle points. These zero-gradient points are connected by minimal-scalar-gradient lines which continuously stretch at rates of order γ, becoming longer than the viscous scale L_K. For $Pr < 1$, this extends the influence of the local rate of strain to lengths of at least the order of the inertial–diffusive scale $L_C > L_K$; that is, larger than the maximum assumed possible by Batchelor, Howells & Townsend (1959). Roughly orthogonal maximal-scalar-gradient lines are also embedded in the fluid, and compressive mixing along these lines also reflects the magnitude and direction of the local rate of strain over distances larger than L_K. Because the two rate-of-strain mixing mechanisms act along lines, they can be modelled by one-dimensional numerical simulation. Both are Prandtl-number independent and together they provide a plausible physical basis for the universal scalar similarity hypothesis of Gibson (1968b) that turbulent mixing depends on γ for all Pr.

1. Introduction

An important property of turbulence is its ability to mix and diffuse scalar fields such as temperature and chemical species concentration. Many processes of practical importance such as chemical reactions and propagation of acoustic and electro-magnetic waves in turbulent media depend on turbulent mixing and diffusion. Unfortunately, no clear understanding of the basic mechanisms of turbulent mixing has emerged even for the simplest case of dynamically passive, non-reacting scalars. The area of greatest disagreement is where the scalar is strongly diffusive. We shall investigate this problem in the following using numerical simulations.

The first attempts to describe turbulent mixing were intuitive extensions of the Kolmogorov (1941) universal similarity hypotheses, based on dimensional analysis. Obukhov (1949) and Corrsin (1951) independently suggest that the scalar diffusive microscale should be $L_C = (D^3/\epsilon)^{\frac{1}{4}}$ by analogy with the Kolmogorov viscous microscale $L_K = (\nu^3/\epsilon)^{\frac{1}{4}}$, where D is the molecular diffusivity of the scalar, ϵ is the

viscous dissipation rate and ν is the kinematic viscosity of the fluid. No physical mechanisms are proposed in these papers to justify L_C as the diffusive microscale.

1.1. *Physical mechanisms of turbulent mixing*

Batchelor (1959) was the first to propose a specific physical mechanism of small-scale turbulent mixing. For weakly diffusive passive scalars, with Prandtl number $Pr \equiv \nu/D > 1$, Batchelor (1959) suggests that scalar wavenumber vectors with wavelength $\lambda < L_K$ should align with the compression axes of the local strain-rate tensor and be convected rapidly to higher wavenumbers by the compressive strain until λ decreases to a diffusive scale $\approx (D/\gamma)^{\frac{1}{2}}$, where γ is some characteristic rate of strain of the turbulence. Because the strain rate is uniform over regions of size L_K and because the smallest scalar wavelengths should be on scales smaller than L_K, the small-scale mixing mechanism envisaged is a compression of scalar wave crests by the local strain field. An analytic expression

$$\phi = \frac{\chi}{|\gamma_3| k} \exp \frac{-Dk^2}{|\gamma_3|}$$

is deduced for the scalar spectrum ϕ with viscous–convective subrange $\sim k^{-1}$ and with exponential cutoff at a diffusive (Batchelor length) scale $L_B = (D/\gamma)^{\frac{1}{2}}$, where $\chi \equiv 2D(\nabla\theta)^2$ is the dissipation rate of scalar fluctuations, the rate-of-strain parameter $\gamma = (\epsilon/\nu)^{\frac{1}{2}}$, and $|\gamma_3|$ is the mean compressive rate-of-strain magnitude. The form of the Batchelor spectrum for $Pr > 1$ has now been confirmed by several independent investigations, starting with Gibson & Schwarz (1963), and the universal proportionality constant $\beta_B \equiv \gamma/|\gamma_3|$ is known to within about 30% accuracy.

For strongly diffusive scalars, with $Pr \ll 1$, Batchelor, Howells & Townsend (1959) propose that the strain rate is irrelevant to the small-scale mixing because the smallest scalar wave-crest separation is much larger than the scale of uniform strain rate $L_K = L_B Pr^{\frac{1}{2}}$, so that the wave-crest compression mechanism of Batchelor (1959) fails: it is impossible to fit the highest-wavenumber scalar Fourier elements into regions of uniform strain rate so the wave crests cannot be convected together by compressive straining. A strong diffusive cutoff of the scalar spectrum at the Corrsin scale L_C is predicted, with an inertial diffusive subrange proportional to $k^{-\frac{17}{3}}$ for scales $L_C \gg L \gg L_K$. Similar arguments are applied to explain the turbulent mixing of weak magnetic fields with magnetic Prandtl numbers less than unity by Moffatt (1961, 1962), Golitsyn (1960) and Kraichnan & Nagarajan (1967), giving similar predictions for magnetic spectral forms with strong diffusive cutoff at L_C.

However, Gibson (1968a) proposes that other mechanisms may exist for $Pr < 1$ (and $Pr \geq 1$) which produce coupling between turbulent scalar fields and the local strain rate but which do not require that the smallest scalar wave-crest separation L_B be smaller than the size of regions of uniform strain rate L_K. Using expressions, discussed in the next section, for the velocities of isoscalar surfaces and the velocities of points, lines and surfaces of zero and minimal scalar gradient, Gibson (1968a) shows that the local rate of strain generates scalar microstructure by a hot- and cold-spot pinching and stretching mechanism that may be independent of Prandtl number. Because scalar extrema are generated if turbulent eddies larger than $L_C = L_K Pr^{-\frac{3}{4}}$ are present, with diffusive time constant $T_C = T_K Pr^{-\frac{1}{2}}$ greater than the convective time constant T_K (see table 2), and because the extremum points tend to move with fluid particles, the strain rate of the fluid particle associated with an extremum point has time to affect the scalar distribution in its vicinity. The scalar diffusive flux and convective flux are complementary in the direction of positive

strain rate and in opposition in the direction of compressive strain rate, so the scalar distribution about the extrema will be distorted in these directions by the fluid motion.

The distortion of the scalar field occurs approximately along lines of maximum stretch and maximum compression to form minimal-gradient lines and maximal-gradient lines, respectively, emanating from the scalar extrema. As the minimal- and maximal-gradient lines form, they move with respect to the fluid and respond to stretch and pinch lines of the local fluid particles as they evolve. All these lines are long compared with L_K. Even though the local rates of strain will tend to decorrelate at distances of L_K along lines selected randomly in the fluid, they need not decorrelate for all lines at such small scales. Because the rate-of-strain magnitude along the maximum-scalar-gradient lines is approximately the local average value γ, the radius of curvature of the scalar distribution should be reduced from L_C to L_B for $Pr < 1$ by the pinching effect of convection in the direction of compressive strain, and the extremum hot spots and cold spots should be stretched by flow in the direction of positive strain. This process is modelled by a one-dimensional numerical simulation in §7 for Pr values as small as 0.001.

Figure 1 (*a*) is a schematic representation of the Batchelor wave-crest-compression mixing mechanism. For $Pr > 1$ the wave-crests of the scalar Fourier element shown in figure 1 (*a*)(i) are compressed together by the straining motion until they are separated by the Batchelor scale L_B. At smaller scales diffusive damping begins and the amplitude of the scalar fluctuation rapidly decreases. For $Pr < 1$ the strain rate varies randomly on scales L_K smaller than L_B or L_C as shown in figure 1 (*a*)(ii), and the Fourier element is unaffected by the rate of strain in the asymptotic limit $Pr \ll 1$ according to the model. Diffusive damping occurs for wavelengths smaller than L_C.

Figure 1 (*b*) illustrates the Gibson (1968*a*) hot-spot pinching and splitting mechanism for $Pr < 1$. The response of an initially uniform scalar-gradient field (dashed lines) to the rotation of a blob of fluid of size L_C is shown in figure 1 (*b*)(i). The strongly distorted isotherms are topologically unstable to molecular diffusion in the sense that the initially singly connected isoscalar surfaces become multiply connected, forming the complex array of extrema and associated saddle points shown in figure 1 (*b*)(ii). For $Pr > 1$, eddies down to the smallest scale permitted by viscous forces (the Kolmogorov scale L_K) can generate extremum points from regions of uniform scalar gradient. For $Pr < 1$, only eddies larger than the Corrsin scale L_C can overcome the diffusive relaxation velocity and produce extrema from uniform gradient regions. For all Pr values, once extrema are produced they tend to move with the fluid and be split repeatedly by the local rates of strain until their separation is L_B, as discussed in Gibson (1968*a*).

As shown in figure 1 (*b*)(ii), minimal-gradient lines pass through strings of positive/negative extrema and their saddle points, and local stretching principal axes will tend to be aligned, giving an average positive rate of strain along the line. As shown in figure 1 (*b*)(iii), maximal-gradient lines form roughly perpendicular to these, with approximately aligned compressive principal rate-of-strain axes and negative average rate of strain along the lines. For $Pr < 1$, the length of such maximal- and minimal-scalar gradient lines should be at least the original eddy size; in this example, the Corrsin length L_C.
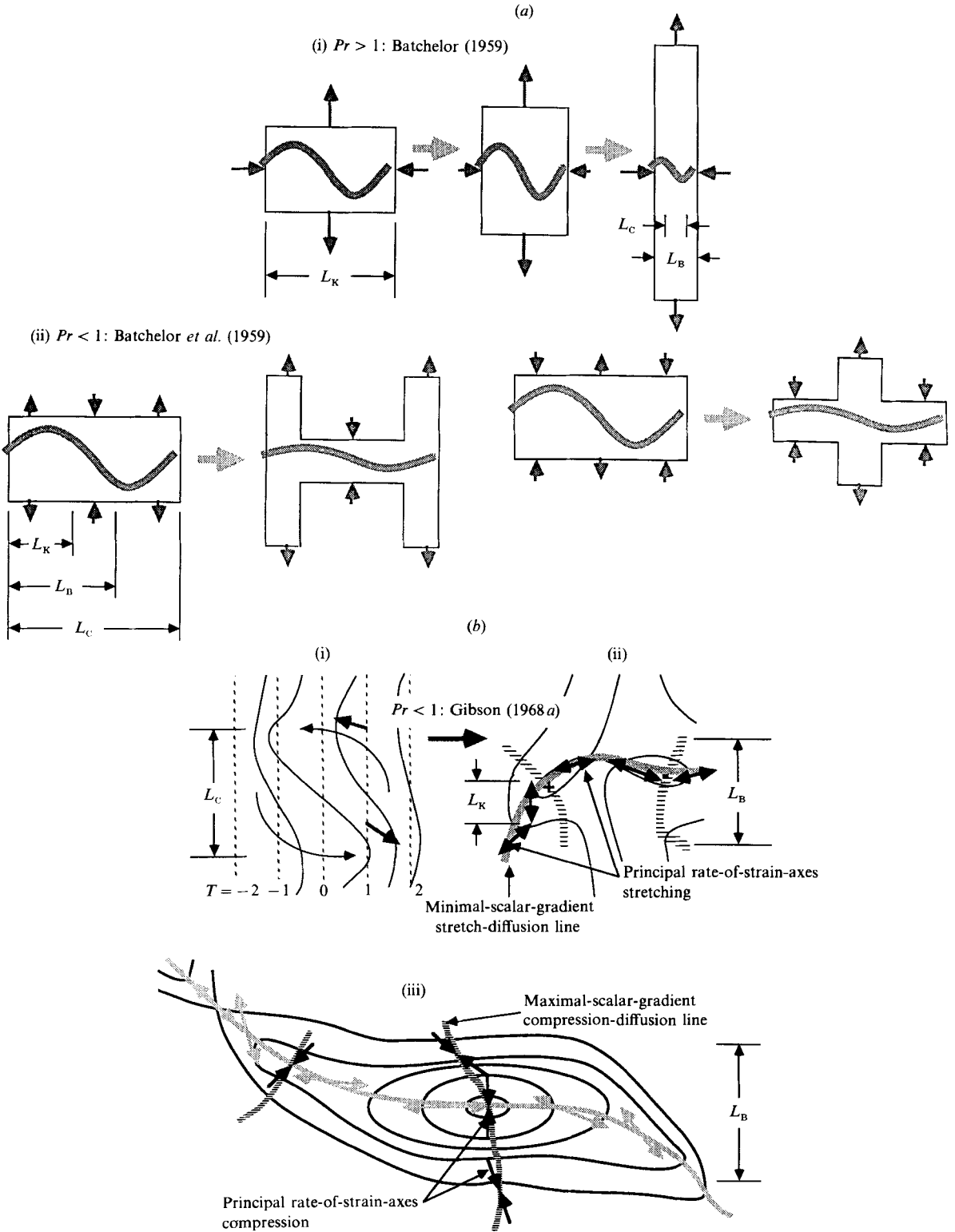
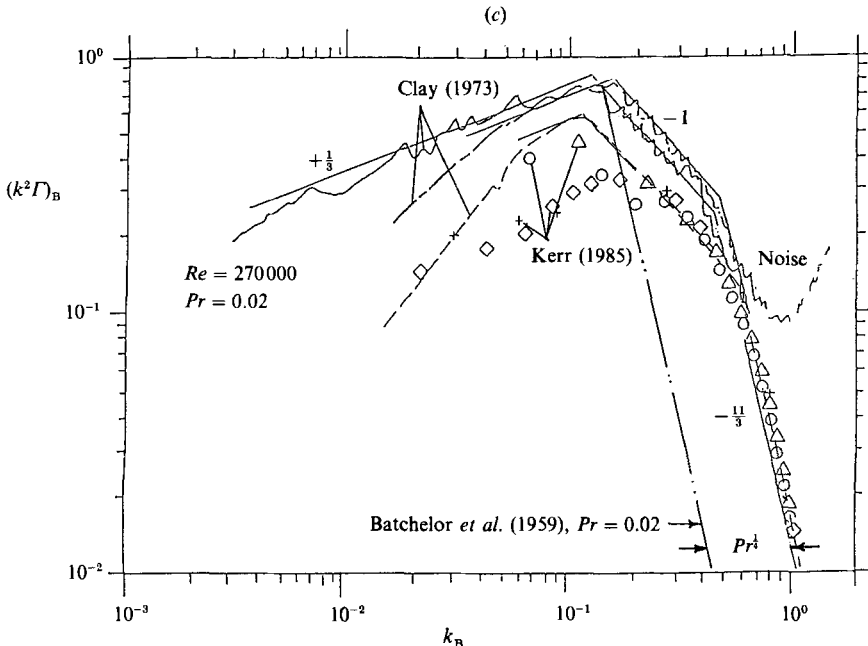FIGURE 1 (*a*, *b*). For caption see facing page.

FIGURE 1. Schematic representations of small-scale turbulent mixing mechanisms. (a) wave-crest-compression mechanism. (i) $Pr > 1$: Batchelor (1959). A rectangular cross-section fluid element of size $\approx L_K$ is distorted by uniform strain. The embedded scalar Fourier element aligns with the compression principal axis and its wavelength is reduced to the Batchelor scale $L_B < L_K$ where the amplitude of the scalar fluctuation begins to decrease owing to molecular diffusion. (ii) $Pr < 1$: Batchelor *et al.* (1959). The rectangular fluid element with length equal to $L_C > L_B > L_K$ is distorted to H and plus shapes for different distributions of strain directions (which are assumed to fluctuate randomly along the axis of the Fourier element). Because the wave crest separation of the Fourier element is larger than the size of the regions of uniform strain L_K the rate of strain has little effect on either the wavelength or the amplitude. Diffusive damping reduces the amplitude of scalar fluctuations of wavelength smaller than L_C.

(b) Rate-of-strain mixing mechanism for $Pr < 1$: Gibson (1968a). (i) Convection of uniform scalar gradient. A fluid blob of scale L_C rotates in an initially uniform gradient field, with dashed-line isotherms. The distorted isoscalar surfaces are shown by solid lines. (ii) Stretching on a minimal-gradient line. Strongly distorted isothermal surfaces are topologically unstable and become multiply connected by molecular diffusion, forming a hot-spot extremum shown by the plus, a cold-spot extremum shown by the minus, and associated saddle points. These zero-gradient points tend to move with the fluid and align with the stretching rate-of-strain-tensor principal axes for scalars of arbitrary Pr, as discussed in the text. A minimal-scalar-gradient line (shaded) connects the extrema and saddle points, and is approximately aligned with local stretching axes. (iii) Compressive straining on maximal-gradient lines. Maximal-scalar-gradient lines (horizontal bar shading in (ii) and (iii)) form in directions roughly orthogonal to the minimal-gradient lines. Compression principal axes are approximately aligned along the lengths of these compression-diffusion lines, and cause the increased gradients.

(c) Temperature dissipation spectra for $Pr \ll 1$. Temperature dissipation spectra for mercury ($Pr = 0.02$) from Clay (1973) compared to numerical simulation data of Kerr (1985), normalized with Batchelor scales indicated by B subscripts (from Gibson & Kerr 1988, figure 4b). ——, ———, ———— are for mercury at Reynolds numbers of $Re_\lambda \approx 520$, 250 and 150, respectively (the upturn for 520 is noise). Symbols are from Kerr (1985) simulations. $\bigcirc$, $\triangle$, $Pr = 0.1$ at Re_λ 83 and 56, respectively; $+$, $\diamondsuit$, $Pr = 0.5$ and 1.0, respectively. —·—·— is the theory of Batchelor *et al.* (1959) for $Pr = 0.02$. The $-\frac{11}{3}$ subrange begins near $\approx L_B^{-1}$ rather than $\approx L_C^{-1}$, reflecting rate-of-strain mixing for $Pr \ll 1$, and is displaced by a factor of $Pr^{-\frac{3}{4}} = 2.7$.

1.2. *Universal similarity hypotheses*

Based on the hot-spot pinching mechanism just described, several universal similarity hypotheses for scalar mixing in different Prandtl-number regimes were proposed by Gibson (1968b). These hypotheses are summarized in table 1, along with the corresponding Kolmogorov (1941) universal similarity hypotheses for high-Reynolds-number turbulent velocity fields.

In table 1, F_n and $F_{\theta n}$ represent the $3n$-joint and n-joint probability laws for velocity differences and scalar (θ) differences, respectively, for separation vectors with magnitude y_k (where $k = 1, ..., n$), using the same nomenclature as Kolmogorov (1941) and Gibson (1968a, b). Velocity hypothesis 1 predicts a universal velocity spectral form with viscous cutoff at the Kolmogorov lengthscale after a coordinate transformation to dimensionless coordinates normalized by length and time scales L_K and T_K formed from ϵ and ν. Scalar hypothesis 1 (a) predicts a universal scalar spectral form, independent of Pr, with diffusive cutoff at the Batchelor scale after a coordinate transformation to dimensionless coordinates normalized by length, time and scalar scales L_B, T_B and S_B formed from χ, γ and D. Dimensional analysis and velocity hypothesis 2 gives the $k^{-\frac{5}{3}}$ inertial subrange and scalar hypothesis 1 (b) gives the $k^{-\frac{5}{3}}$ scalar inertial subrange. Scalar hypothesis 2 (b) leads to a new inertial–diffusive subrange proportional to k^{-3}. Hypothesis 3 (b) requires the viscous–convective k^{-1} subrange predicted by Batchelor (1959). Length-scales for the various spectral subranges are given in table 1.

Transformation to dimensionless coordinates in three universal similarity spaces is accomplished with Batchelor, Corrsin and Kolmogorov length, time and scalar similarity scales required by scalar hypotheses 1 (a), 2 (a) and 3 (a) in table 1, as discussed in Gibson (1968b). The resulting scalar similarity scales are listed in table 2.

1.3. *Experimental and numerical evidence for scalar hypothesis 1 (a)*

Clay (1973) measures spectra and other statistical parameters of temperature in turbulent mercury. The inertial–diffusive subrange indicated by Clay's measurements is $\sim k^{-3}$ for $L_C > L > L_B$ and $\sim k^{-\frac{17}{3}}$ for $L_B > L > L_K$, which is consistent with both the prediction of Gibson (1968b), using hypothesis 2 (b) of table 1, and the prediction of Batchelor *et al.* (1959), except with a smaller range of lengthscales. Clay measures the strain-rate–scalar-dissipation correlation coefficient,

$$\Sigma = \frac{\langle u_{x,x} T_{,x}^2 \rangle}{\langle u_{x,x}^2 \rangle^{\frac{1}{2}} \langle T_{,x}^2 \rangle}, \tag{1}$$

for turbulent temperature fluctuations in mercury, air and water, with Prandtl numbers of 0.02, 0.7 and 7, respectively. In all cases he finds Σ values of about -0.4. As discussed in §3, the Batchelor *et al.* (1959) spectral theory indicates a rapid decrease of Σ to zero as Pr decreases below unity, whereas the Gibson (1968b) spectral theory predicts a nearly constant value of -0.5 independent of Pr. Kerr (1985) finds $\Sigma = -0.5$ for three-dimensional numerical turbulent mixing of scalars with $Pr = 0.1$, 0.5, 1.0 and 2. The negative sign of the correlation reflects the enhancement of scalar gradients in the direction of compressive straining, where $u_{x,x}$ is negative, and a decrease in scalar gradients in the stretching direction, where $u_{x,x}$ is positive (subscripts preceded by a comma denote partial derivatives that have precedence over exponents: thus $u_{x,x}$ is $\partial u_x / \partial x$ and $T_{,x}^2$ is $(\partial T / \partial x)^2$).

Figure 1 (c), from Gibson & Kerr (1988, figure 4b), shows that spectra of Clay (1973) and Kerr (1985) collapse to the same spectral level under Batchelor scaling

Field		Hypothesis	Length range	Pr
Velocity	1.	$F_n(\epsilon, \nu, y_k)$	$y_k < L_0$	na
	2.	$F_n(\epsilon, y_k)$	$L_K < y_k$	na
Scalar	1 (a).	$F_{\theta n}(\chi, \gamma, D, y_k)$	$y_k < L_B$	all
			$y_k < L_K$	> 1
			$y_k < L_C$	< 1
	1 (b).	$F_{\theta n}(\chi, \epsilon, y_k)$	$L_K < y_k < L_0$	> 1
			$L_C < y_k < L_0$	< 1
	2 (a).	$F_{\theta n}(\chi, \epsilon, D, y_k)$	$L_B < y_k < L_0$	< 1
	2 (b).	$F_{\theta n}(\chi, D, y_k)$	$L_B < y_k < L_C$	< 1
	3 (a).	$F_{\theta n}(\chi, \epsilon, \nu, y_k)$	$L_B < y_k < L_0$	> 1
	3 (b).	$F_{\theta n}(\chi, \gamma, y_k)$	$L_B < y_k < L_K$	> 1

TABLE 1. Universal similarity hypotheses for turbulence and turbulent mixing

Scale	Batchelor	Corrsin	Kolmogorov
Length	$(D/\gamma)^{\frac{1}{2}}$	$(D/\gamma\, Pr^{\frac{1}{2}})^{\frac{1}{2}}$	$(\nu/\gamma)^{\frac{1}{2}}$
Time	γ^{-1}	$(\gamma\, Pr^{\frac{1}{2}})^{-1}$	γ^{-1}
Scalar	$(\chi/\gamma)^{\frac{1}{2}}$	$(\chi/\gamma\, Pr^{\frac{1}{2}})^{\frac{1}{2}}$	$(\chi/\gamma)^{\frac{1}{2}}$

TABLE 2. Scalar similarity scales

near $kL_B \approx 0.5$ for the full range of $Pr < 1$ values considered. The dash-dot-dot line shows the $-\frac{17}{3}$ subrange predicted by the Batchelor *et al.* (1959) theory, which starts from $k \approx L_C^{-1}$ rather than $k \approx L_B^{-1}$ as shown by the data. For mercury, the displacement is by a factor of $Pr^{-\frac{1}{4}} = 2.7$, as shown. This spectral convergence with rate-of-strain scaling and the constancy of computer and laboratory $\varSigma$ values near -0.5 support the Gibson (1968a, b) proposal that the local strain rate should be relevant to small-scale scalar mixing for all Prandtl numbers. However, more detailed study is required to reveal the precise physical mechanism or mechanisms of the observed Pr-independent rate-of-strain mixing.

1.4. *Numerical simulation of turbulent mixing*

Numerical turbulent mixing studies have recently become feasible with the advent of higher speed machines and efficient computational algorithms which can simulate turbulent flows at sufficiently high Reynolds number to be relevant. The nature of the numerical approach to turbulent mixing is well suited to studies of detailed mixing mechanisms since complete characterization of the velocity and scalar fields is available for each mesh point of the computational grid. Laboratory studies at low Pr values can be done by measuring temperature fluctuations in liquid metals. However, hot-film-anemometer spatial resolution is seriously degraded by the strong thermal diffusivity in liquid metals; additionally, velocity and temperature sensors must be carefully insulated electrically by coating materials to avoid shorting through the metal. Mercury is expensive and poisonous, and molten NaK alloys burn on contact with air. As an alternative, free-electron concentration in weakly ionized turbulent plasmas is convected as a strongly diffusive passive scalar, with $Pr < 1$, and may be studied by electromagnetic-wave scattering. However, scattering studies tend to reveal only averaged scalar structure such as spectra rather than mixing mechanisms. Computer studies for $Pr < 1$ may actually be easier than for $Pr > 1$

because the scalar diffusive cutoff occurs at larger lengthscales for a given velocity field, permitting use of fewer mesh cells in the computation to resolve the scalar field.

In the following we analyse the results of a numerical turbulence-mixing simulation at low Prandtl number in an attempt to identify the physical mechanisms by which the strain-rate field becomes correlated with the rate of scalar dissipation, as observed by Clay (1973) and Kerr (1985). Kerstein & Ashurst (1984) used a numerical two-dimensional homogeneous mixing simulation to investigate the lognormal properties of the scalar dissipation rate $\chi \equiv 2D(\nabla\theta)^2$ (a factor of 2 has been included to make the definition of χ consistent with that of Batchelor 1959). The resulting computed velocity and scalar fields were saved, and are used in the present paper to study the mechanisms of strain-rate interaction with the scalar field. The study supports the Gibson (1968a) hot-spot pinching mechanism, but reveals a new, and unanticipated, interaction mechanism which occurs where the scalar gradients are large rather than small.

Finally, low-Prandtl-number diffusion and convection along the stretch and pinch lines described above is analysed by a one-dimensional numerical simulation of high-Reynolds-number turbulent mixing in §7.

2. Kinematics of scalar mixing

Following the Batchelor (1959) approach, we consider a dynamically passive scalar field like temperature mixed by an incompressible Newtonian fluid. Denoting the scalar as $T(x,t)$

$$T_{,t} + u \cdot \nabla T = D\nabla^2 T, \tag{2}$$

where $T_{,t}$ is the partial derivative of T with respect to time t, x is the position in space and u is the velocity field. Both T and u are assumed to have zero mean values.

Gibson (1968a) derives an expression for the velocity of an isoscalar surface at any point in the fluid

$$u^T = u - D\left(\frac{\nabla^2 T}{|\nabla T|}\right)g, \tag{3}$$

where D is the molecular diffusivity of T and g is the unit vector of ∇T. The second term on the right is the diffusion velocity, i.e. the velocity of the isoscalar surface at any point with respect to the fluid velocity.

Equation (3) is derived by expanding $T(x,t)$ using the chain rule

$$dT = T_{,j}\,dx_j + T_{,t}\,dt.$$

This is zero on an isothermal surface, and on this surface $dx_j = u_j^T\,dt$. Combining with (2) gives

$$T_{,j}(u_j^T - u_j) = -DT_{,jj},$$

which is

$$= |T_{,j}|\,|u_j^T - u_j|$$

since the isothermal velocity relative to the fluid, $u^T - u$, is parallel to the scalar gradient ∇T. The vector form of this is (3), an expression that is very useful in describing the response of a scalar field to convection and molecular diffusion.

We can identify several modes of response, or lack of response, of the scalar field to fluid convection using (3):

(i) When $D = 0$, corresponding to a non-diffusive scalar such as dye in liquid, we see that the scalar follows the fluid precisely; that is, $u^T = u$.

(ii) When D is non-zero the diffusion velocity v_D may be larger in magnitude than the fluid velocity, depending on the ratio $\nabla^2 T/|\nabla T| \approx 1/L$. For turbulence acting on a uniform gradient scalar field, it follows from (3) that the diffusion velocity $v_D \approx D/L$ dominates the convective velocity $v_C \approx (\epsilon L)^{\frac{1}{3}}$ for eddies with lengthscale L smaller than the Corrsin scale L_C, as shown by Gibson (1968a). For $Pr > 1$, eddy velocities at all lengthscales $(L > L_K > L_C)$ are larger than the diffusion velocity. For $Pr < 1$, only eddies with $L > L_C$ have $v_C > v_D$.

(iii) When $|\nabla T|$ approaches zero the diffusion velocity approaches infinity. Strongly distorted isoscalar surfaces can become unstable and then multiply connected owing to the formation of new isolated extrema, as shown by Gibson (1968a) and figure 1(b).

(iv) When the ratio $\nabla^2 T/|\nabla T|$ is small the diffusion velocity may also be small even though D is large. This provides a new mechanism for the local strain rate to strongly influence the scalar microstructure even when $Pr < 1$. Because the ratio will tend to be small where $|\nabla T|$ is large, compressive pinching of the local scalar gradients can be most effective at aligning and amplifying local scalar gradients just where the mixing is greatest, thus increasing the gradient and further decreasing the ratio in a positive feedback process.

Gibson (1968a) derives the following expression for the velocity of points in the fluid with zero scalar gradient:

$$\boldsymbol{u}^0 = \boldsymbol{u} - D\left[\left(\frac{T_{,jj1}}{T_{,11}}\right), \left(\frac{T_{,jj2}}{T_{,22}}\right), \left(\frac{T_{,jj3}}{T_{,33}}\right)\right], \tag{4}$$

where the coordinate system is aligned with the principal axes of the tensor $T_{,ij}$ with principal values given by $T_{,11}$ etc., $T_{,jj}$ represents $\nabla^2 T$, and $T_{,jj1}$ etc. are the components of the vector $\nabla(T_{,jj})$. Equation (4) shows that extrema diffuse toward positions of symmetry, where $\nabla(T_{,jj}) = 0$. The diffusion velocity of zero-gradient points with respect to the fluid velocity $\boldsymbol{u}$ is given by the second term on the right-hand side of (4). When extrema achieve a nearly symmetric shape they are convected nearly as fluid particles if their $T_{,ij}$ principal values are large, as they will tend to be for newly created extrema. When the point is near the end of its lifetime it can diffuse very rapidly because the principal values of $T_{,ij}$ approach zero, and the extremum will find and annihilate with its zero-gradient saddle point, which also will have a large diffusion velocity for the same reason, according to (4). Zero-gradient points lie on unique minimal-gradient surfaces which also tend to move with the fluid, and are stretched, pinched and aligned with the local rate of strain, as shown by Gibson (1968a). Stretching along lines that lie in minimal-gradient surfaces may occur over distances much larger than the viscous scale L_K, as discussed previously.

3. The strain-rate–scalar-dissipation correlation coefficient

The strain-rate–scalar-dissipation correlation coefficient Σ, defined in (1), provides a powerful statistic for detecting the influence of fluid straining on the scalar dissipation rate χ. Wyngaard (1971) derives several useful relations involving Σ, including the following expression for computing Σ from the integral of the high-wavenumber scalar spectrum:

$$\Sigma = -(4/5)\,15^{\frac{1}{2}} \int_0^\infty k_B^4\,\phi_B\,\mathrm{d}k_B, \tag{5}$$

where ϕ is the one-dimensional scalar spectrum and the subscript B indicates scaling with Batchelor length, scalar and time scales.
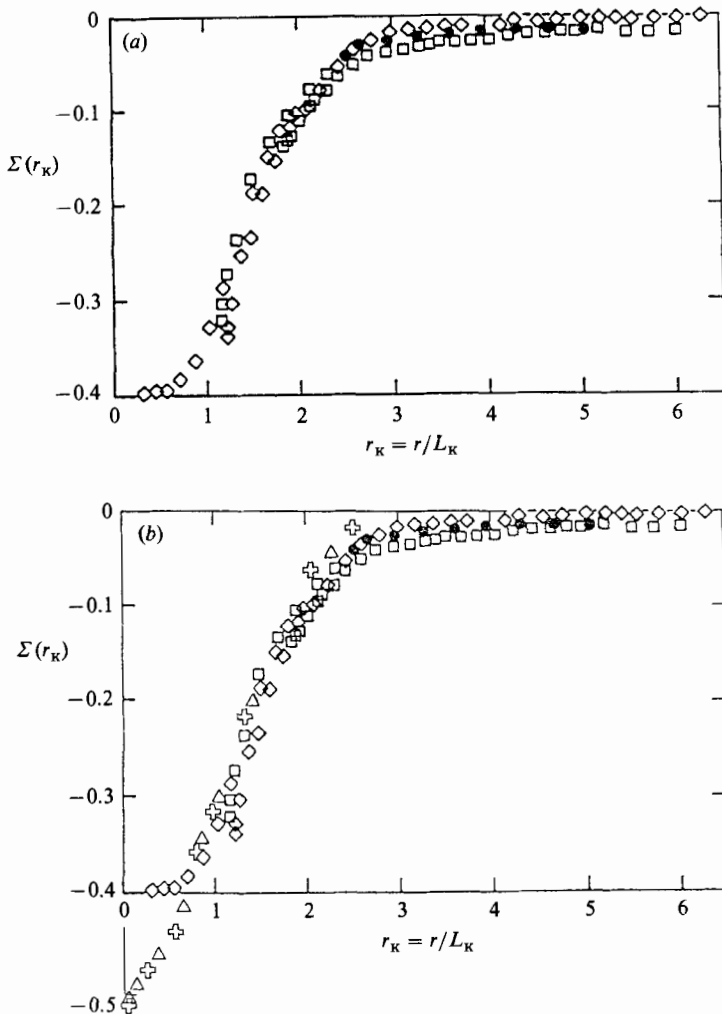
FIGURE 2. (a) Local strain-rate–scalar-dissipation correlation coefficient versus probe separation. $\Sigma(r/L_K)$ values measured by Clay (1973) in mercury, air and water by time delay δt, setting $r = u \times \delta t$ based on Taylor's hypothesis, where u is the velocity. (b) Same data as (a) compared to numerical simulation data of Kerr (1985) computed by William Ashurst (from Gibson & Kerr 1988, figure 6). ●, Hg, $Pr \approx 0.02$, grid; ◇, air, $Pr \approx 0.7$, over ocean; □, H_2O, $Pr \approx 7.0$, sphere wake. Numerical: △, $Pr = 0.1$; ✛, $Pr = 0.5$.

$$\Sigma(r) \equiv \frac{\overline{\left(\dfrac{\partial u_x}{\partial x}\right)_x \left(\dfrac{\partial T'}{\partial x}\right)_{x+r}^2}}{\left[\overline{\left(\dfrac{\partial u_x}{\partial x}\right)^2}\right]^{\frac{1}{2}} \overline{\left(\dfrac{\partial T}{\partial x}\right)^2}} .$$

Figure 2(a) is a plot of the two-point correlation $\Sigma(r)$ between the streamwise straining $u_{x,x}$ and the streamwise temperature gradient squared $T^2_{,x}$ at a point separated by a distance r along the x-coordinate, measured by Clay (1973) in mercury, air and water, as a function of r normalized by the Kolmogorov scale L_K. Strong negative correlation begins at $r = 2.5L_K$ for all three Prandtl-number fluids with $\Sigma(r)$ less than -0.3 for air and water for $r = L_K$, and $\Sigma(0)$ less than -0.4 for
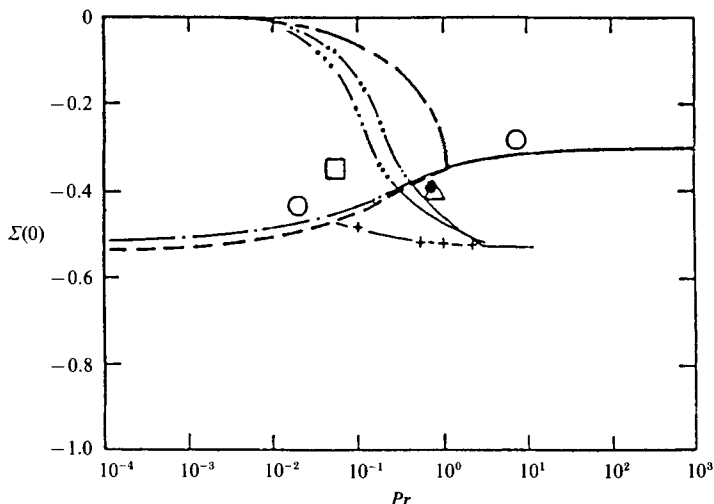
FIGURE 3. Σ versus Pr from theories and measurements. Open symbols are values inferred from spectral measurements using the integral expression of equation (5): $\bigcirc$ = mercury, water, from Clay (1973); $\square$ = plasma, from Granatstein, Buchsbaum & Bugnolo (1971); $\triangle$, air, from Boston (1970). Direct measurement: $\bullet$, air, from Clay (1973). Three-dimensional numerical simulation by Kerr (1985), +. Numerical models: ——·——, model No. 4 of Hill (1978); ——·····——, Larcheveque *et al.* (1980). Theories: ————, Batchelor (1959); ———, Batchelor *et al.* (1959); ——·——, Clay (1973); ————, Gibson (1968a).

air. Instrumental difficulties prevented measurements for separations less than $r = 2.3L_{\mathrm{K}}$ for mercury, and less than $r = L_{\mathrm{K}}$ for water. Recent analysis of the Kerr (1985) numerical simulation data by Ashurst, reported by Gibson & Kerr (1988, figure 6), are in good agreement with figure 2(a), as shown in figure 2(b) for $Pr = 0.1$ (triangles), and $Pr = 0.5$ (crosses).

Figure 2 shows that the local strain produces scalar gradients on very small scales indeed when one recalls that the viscous cutoff of the universal turbulent velocity spectrum begins at about $k = 0.1L_{\mathrm{K}}^{-1}$ which is a wavelength of $60L_{\mathrm{K}}$. The highest-wavenumber wave-crest separation for temperature in water should be smaller by a factor of $Pr^{\frac{1}{2}}$, that is, at a scale of about $20L_{\mathrm{K}}$, which is an order of magnitude larger than the scales at which strain rate is strongly correlated with scalar gradient magnitude according to figure 2. Because the same $\Sigma(r/L_{\mathrm{K}})$ curve appears to represent both high- and low-Pr scalars, we have evidence in figure 2 that the same mixing mechanism may dominate in all cases, and that it is *not* wave-crest compression. Decorrelation occurs for $r \approx (1-2)L_{\mathrm{K}}$.

Figure 3 compares Σ values for various theories and experiments as a function of Pr. The curves for Batchelor *et al.* (1959), Batchelor (1959), Clay (1973), and Gibson (1968b) are computed from predicted theoretical curves using (5), the open circles are computed from measured spectra, and the solid point represents the only direct measurement, from figure 2, by Clay (1973) in air over the ocean. The curves for model No. 4 of Hill (1978) and for a test field model of Larcheveque *et al.* (1980) are taken from Kerr (1985, figure 5) along with Kerr's values computed by three-dimensional numerical simulation. We see from figure 3 that all theories and the laboratory and numerical experiments are in agreement that Σ is about -0.5 for weakly diffusive scalars, with $Pr > 1$. However, the laboratory and numerical data indicate that Σ remains relatively constant for $Pr < 1$, in agreement with the theory

of Gibson (1968*b*), and in disagreement with the theory of Batchelor *et al.* (1959) and the models of Hill (1978) and Larcheveque *et al.* (1980).

4. The two-dimensional numerical mixing system

It seems clear from the evidence of figures 2 and 3 that local strain strongly influences the small-scale structure of turbulent scalar fields at all Prandtl numbers. The remaining questions are: 'By what physical mechanism or mechanisms does the rate-of-strain field interact with the scalar field to produce small-scale structure and enhance mixing ? '; and 'Are the same mechanisms dominant at all Prandtl numbers, providing a physical basis for universal similarity ? '.

As discussed previously, numerical simulations provide many advantages over laboratory experiments in attempting to answer these questions. However, it is important in selecting the numerical scheme to be sure that the small-scale velocity and scalar field interaction mechanisms are not filtered out by any approximations. From figure 3 we see that schemes that approximate the equations of motion, such as Hill (1978) and Larcheveque *et al.* (1980), are inconsistent with measurements of the parameter Σ for $Pr < 1$, whereas more exact numerical simulations at modest Reynolds numbers by Kerr (1985) are in good agreement (the agreement is achieved at considerable computational expense: some 70 hours of computation on a 'super computer'). To study mixing mechanisms that act at very small scales it may be better to have an approximate representation of the large-scale flow but with exact equations, than an exact representation of large-scale features with approximate conservation equations which may obscure the actual small-scale mixing processes.

Kerstein & Ashurst (1984) explore the lognormality of the scalar dissipation rate χ at low Pr in a homogeneous, two-dimensional mixing system using a discrete vortex simulation method developed by Ashurst (1979) and Ashurst & Barr (1983). As predicted by an extension of the Kolmogorov (1962) third universal similarity hypothesis (a refinement of the Kolmogorov hypotheses 1 and 2 in table 1 to account for the increase in intermittency of ϵ and χ with increasing Reynolds number), χ averaged over regions of scale r were found to be lognormal with variance increasing approximately as $\ln(1/r)$ as r decreased to a limiting value $\approx L_B$, the Batchelor scale. This is consistent with the Gibson (1968*a, b*) proposal that the smallest lengthscale for scalars with arbitrary Pr should be L_B.

Details of the computational method are given in the cited references and will not be repeated here, except to note that, because the simulation is two-dimensional, any mixing mechanisms that depend on vortex stretching will not be represented. For each realization of the velocity field, 200 vortices are assigned random locations within a square region of size L. The stream function Ψ_i for each vortex i is given by

$$\Psi_i = \frac{\Gamma_i}{4\pi} \ln(R^2 + R_i^2), \tag{6}$$

where the vortex core size R_i is sampled from a uniform distribution over $(0, R_C)$ and the vorticity strength Γ_i is sampled from a uniform distribution $(-\Gamma, \Gamma)$. In the vortex dynamics algorithm, the vortices advect the scalar, and are themselves advected, by the velocity field that they generate.

A homogeneous scalar gradient is simulated by imposing periodic boundary conditions on the scalar field along the top and bottom edges of the computational region, but imposing jump-periodic boundary conditions on the side edges. Therefore, fluid elements exiting a side edge have their scalar values reduced or increased by LQ

upon re-entering the opposite side, where Q is the imposed scalar gradient. Advection and diffusion of the scalar field are implemented on an 80×80 Eulerian grid with diffusion coefficient chosen to exceed numerical diffusion due to the finite grid, as described by Ashurst & Barr (1983).

Kerstein & Ashurst (1984) verify that the stream-function distribution and scalar distribution have relaxed to statistical stationarity in the realizations used in the following study of local mixing mechanisms. Several combinations of vortex core size and circulation are computed. In the following we examine eight realizations of their Case 1: the case with smallest core size and maximum circulation strength. Figures 4–8 illustrate only one of the eight realizations.

Case 1 was chosen because it is most locally isotropic and shows the greatest variance of scalar and velocity dissipation rates of the available combinations, so that it seemed most representative of the local scalar and velocity structure of stationary high-Reynolds-number turbulence. One measure of the Reynolds number of a turbulent flow is the variance of the natural logarithm of the local dissipation rates: $\mathrm{var}(\ln \chi) = \mathrm{var}(\ln T^2_{,x})$ or $\mathrm{var}(\ln \epsilon) = \mathrm{var}(\ln u^2_{x,x})$. Values of these quantities were computed for Case 1, and were found to be 3.0 and 2.8, respectively, corresponding to values that might be obtained in high-Reynolds-number laboratory flows or low-Reynolds-number atmospheric boundary-layer flows.

Because the simulation of the velocity field has no kinematic viscosity coefficient ν we must estimate an effective Prandtl number of the simulation indirectly. One method is to compare the high-wavenumber cutoff wavelengths λ of the velocity and scalar fields since the ratio should be approximately equal to $Pr^{\frac{1}{2}}$, that is,

$$\lambda_u/\lambda_T = L_\mathrm{K}/L_\mathrm{B} = Pr^{\frac{1}{2}} \tag{7}$$

for all Pr values according to the Gibson (1968a, b) theory and equal to $L_\mathrm{K}/L_\mathrm{C} = Pr^{\frac{3}{4}}$ for $Pr < 1$ if the diffusive cutoff were at L_C rather than L_B, as postulated by Batchelor *et al.* (1959). An approximate version of this method of estimating the Prandtl number is to compare the number of scalar and vorticity (or stream-function) extrema.

Figure 4(*a*, *b*) shows the locations of scalar and stream-function maxima and minima for one realization of the simulated mixing flow field after statistical equilibrium has been achieved. The extrema are located by comparison of a cell value with its eight neighbouring values. We see that there is more fine structure in the velocity field than in the scalar field, with 86 stream-function extrema compared to only 15 hot and cold spots. The number of extrema is inversely proportional to the square of their mean separation distance so the effective Prandtl number must be substantially less than one, and approximately equal to the ratio of scalar spots to vorticity spots from (7); that is, $Pr \approx 0.2$.

A qualitative demonstration that the simulated Prandtl number is small is given by figure 4(*c*), which is a plot of u_x, the x-component of velocity $\boldsymbol{u}$, and the scalar value T as a function of x at a constant value of $y = 0.5$: a horizontal cut through the midsection of figure 4(*a*, *b*). Notice the finer scale of variation of the velocity signal compared with that of the scalar field, indicating that the Prandtl number is less than unity. Also note the equality of u_x values at $x = 0$ and $x = 1.0$ and the imposed scalar gradient in the T plot, required by the jump-periodic boundary condition.

For a better approximation of the wavelength ratio in (7), average distances between zero crossings were computed for $T_{,x}$ and for $u_{x,x}$ (and $T_{,y}$ and $u_{y,y}$) for the eight realizations giving $Pr = 0.3$, from (7), or 0.05 if the scalar diffusive cutoff is
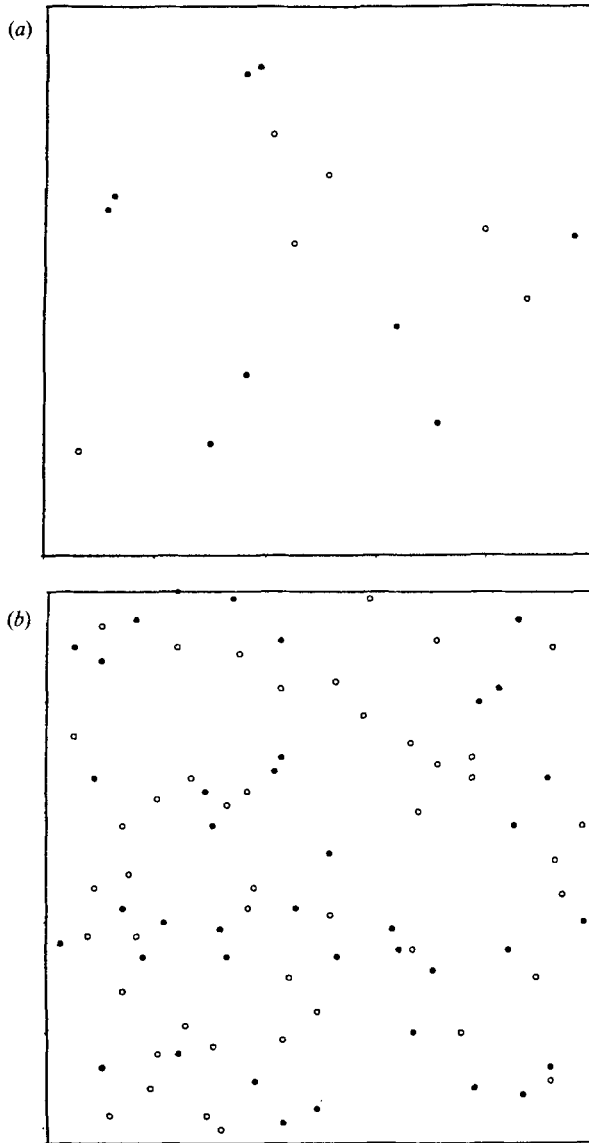
FIGURE 4 (a, b). For caption see facing page.

assumed to be at L_C rather than L_B. Thus, by all methods of estimation, the effective Prandtl number is substantially less than one, which is the case of interest.

5. Results of the simulation

To examine the interaction of the rate-of-strain field with the scalar-gradient field, unit vectors were computed at each mesh point of the 80×80 grid pointing in the direction of the positive principal strain axes x_1 and with length equal to the diagonal size of a mesh cell, as shown in figure 5 (a). Unit vectors pointing in the direction of the scalar gradient are shown in figure 5 (b). Comparison of figure 5 (a) with figure 5 (b) shows that the regions of uniform scalar-gradient direction are often the same size
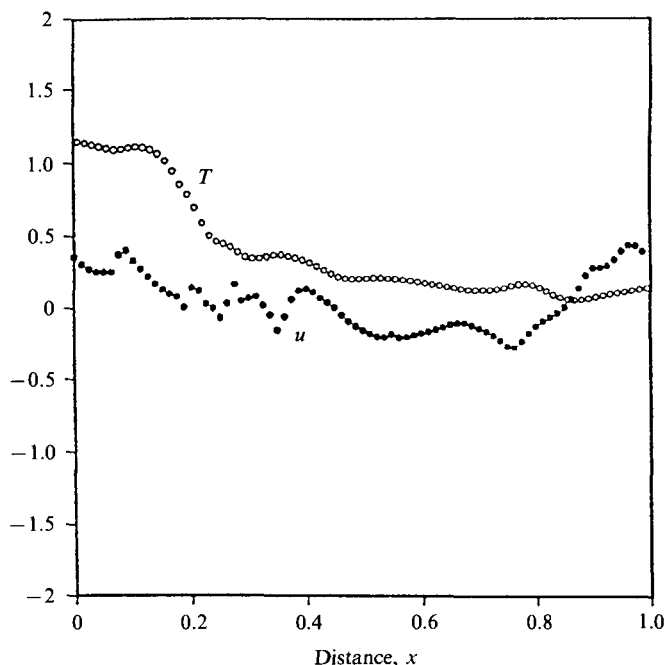
FIGURE 4. Evidence that Pr for the two-dimensional simulation is less than 1. (*a*) Scalar extrema. (*b*) Stream function extrema (maxima are solid circles and minima are open circles). (*c*) $u(x, y = 0.5)$ and $T(x, y = 0.5)$. Note that for (*a*), (*b*) and (*c*) the scalar field has less small-scale structure than the velocity field, indicating $Pr < 1$.

and in the same location as the regions of uniform strain-rate direction, rather than being randomly distributed in space and a factor of $L_B/L_K = 2.8$ larger, which is the ratio computed previously. It would appear that the scalar-gradient field is responding to the rate-of-strain field. Qualitative confirmation of this conclusion is obtained by overlaying the two fields, which shows that in most locations the vectors are nearly perpendicular, that is, the scalar gradient g is aligned with the direction of compressive straining x_3.

A quantitative measure of the degree of alignment of the scalar-gradient direction with the rate-of-strain direction is shown in figure 6, which is a plot of $g \cos^2 \theta$ vectors at each mesh point, where θ is the angle between the compression axis x_3 of the rate-of-strain field and the unit vector g of the scalar gradient. If the two vectors were randomly oriented the average value of $\cos^2 \theta$ would be 0.5. The actual average value of $\cos^2 \theta$ computed for the eight realizations of the simulated flow field is significantly larger than 0.5: $\langle \cos^2 \theta \rangle = 0.640 \pm 0.003$. The 'strain-rate–gradient alignment' map in figure 6 is compared to the corresponding scalar contour map in figure 9 below.

Computation of the strain-rate–scalar-dissipation correlation coefficient Σ defined by (1) gives an average value for the eight realizations of -0.22 ± 0.01. This value is smaller in magnitude than the values of about -0.4 to -0.5 found by experiments and the Kerr (1985) simulation of three-dimensional turbulent mixing, shown in figure 3, but the negative sign indicates that compressive strain-induced mixing is also taking place in the two-dimensional simulation. Further discussion of the interpretation of these results will be given in the next section.

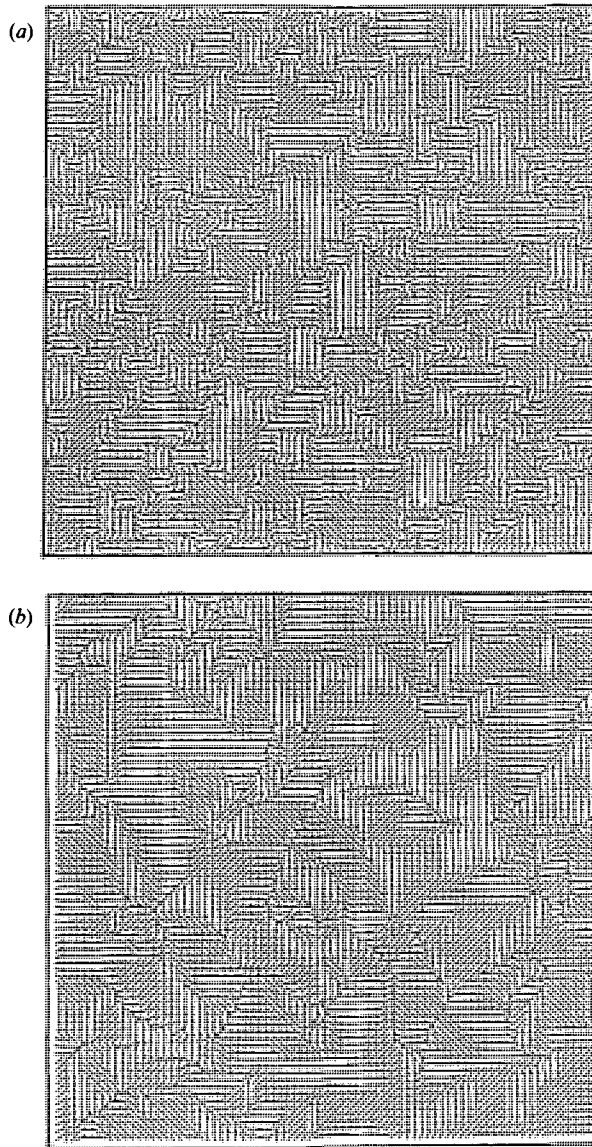Figure 7 is a plot of vectors with length proportional to the local dissipation rate,

FIGURE 5. Maps of positive strain and scalar gradient directions. (a) Positive rate-of-strain x_1.
(b) Scalar gradient g.

i.e. the squared scalar gradient, and with the direction of the local scalar gradient. It shows that the dissipation is not uniformly distributed, but is concentrated in a few elongated regions with width about equal to the size of the regions of uniform strain-rate direction shown in figure 5(a).

Figure 8(a) is a contour map of the scalar field, and may be compared to the dissipation plot of figure 7 and the hot- and cold-spot plot of figure 4(a). Figure 8(b) is an overlay of this contour map with the strain field of figure 5(a), and shows that the ridge lines of the scalar contours generally coincide with the directions of positive strain, as expected from the model of Gibson (1968a) which predicts the stretching of minimal-gradient surfaces by the strain-rate tensor in three-dimensional turbulent
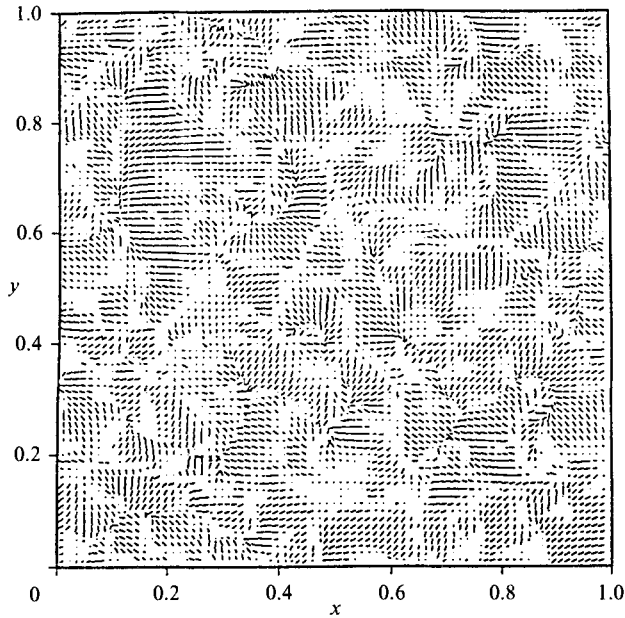
FIGURE 6. Map of strain-rate–scalar-gradient alignment parameter $\cos^2 \theta$, where θ is the angle between the scalar gradient and the compression rate-of-strain axes. The average of $\cos^2 \theta$ is 0.64, versus 0.5 if the directions were oriented at random. The lines are scaled to the $\cos^2 \theta$ value and are in the scalar gradient direction $\boldsymbol{g}$.
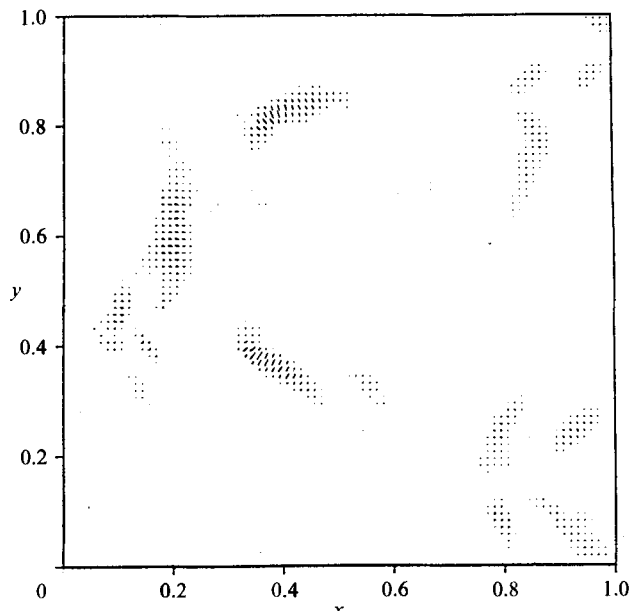
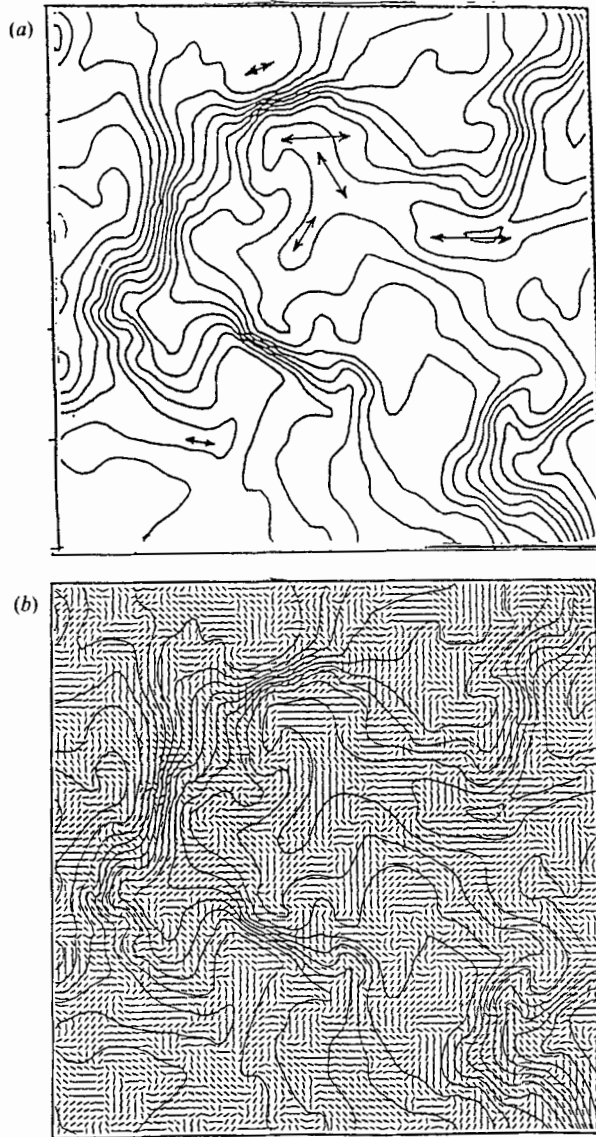FIGURE 7. Scalar dissipation rate. Vectors with length proportional to $|\nabla T|^2$ and direction of ∇T.

FIGURE 8. Scalar field and strain field. (a) Contour map of the scalar field – 20 contours. Arrows indicate the direction and length of the regions of positive rate of strain x_1 on ridge lines. Alignment of x_1 with ridge lines illustrates the effect of strain-rate-mixing mechanism 1. (b) Overlay of (a) with the positive straining field of figure 5(a).

mixing: the two-dimensional analogue is stretching and alignment of contour ridge lines with the directions of positive strain. Strain-induced splitting of extrema by the local strain-rate field was observed by comparing a time sequence of extrema maps such as figure 4(a) overlaid with the corresponding strain-rate fields such as in figure 5(a). Arrows are drawn on some of the contour ridge lines of figure 8(a) showing the alignment of the ridges with the direction and length of the positive strain regions, shown in more detail in figure 8(b). Two pairs of recently split maxima are shown in figure 4(a). These are separated by ridge lines aligned with the positive strain axes, from figure 8(b), as expected from the minimal-gradient stretching mechanism.
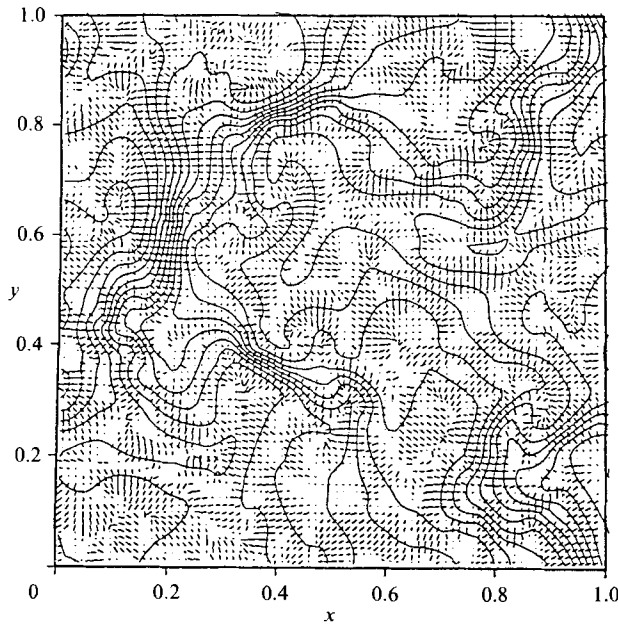
FIGURE 9. Overlay of scalar contour map of figure 8(a) with the strain–gradient alignment map of figure 6. Good alignment where the scalar gradient magnitude is large illustrates the effect of strain-rate-mixing mechanism 2.
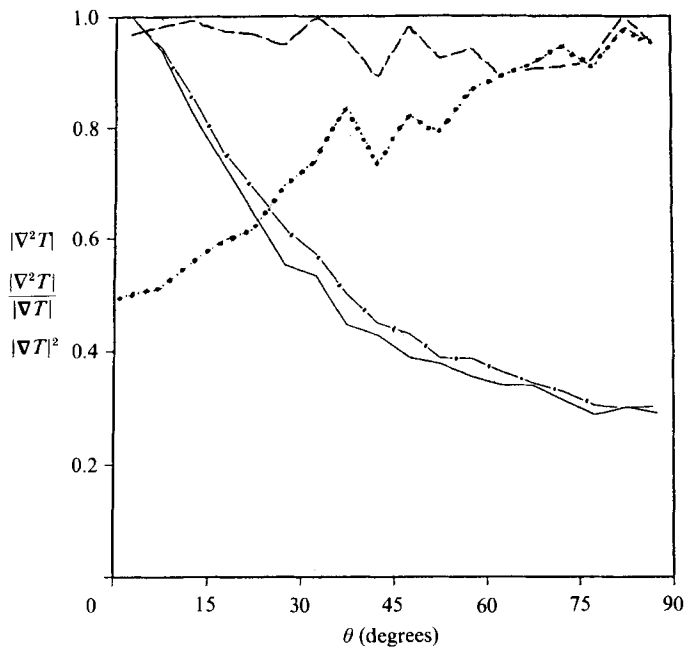

FIGURE 10. Conditioned averages of $|\nabla^2 T|$ (----), $|\nabla^2 T|/|\nabla T|$ ($\cdots\cdots$) and $|\nabla T|^2$ (———); and relative frequency of samples (—·—), versus alignment angle θ between compressive strain x_3 and scalar gradient g directions. The decrease in $|\nabla^2 T|/|\nabla T|\,[\theta]$ as $\theta \to 0$ supports the new 'gradient-pinching' mechanism 2.

Figure 9 shows an overlay of the scalar contours of figure 8(a) with the $\cos^2 \theta$ 'strain–gradient alignment' map of figure 6. All of the regions of maximum dissipation rate coincide with regions of strong strain–gradient alignment, suggesting that the strain may be causing the strong gradient magnitudes by aligning the scalar-gradient directions and amplifying the gradient magnitudes. Overlays similar to figure 9 were carried out for the eight realizations of the simulation and all indicate the same pattern of strong alignment in regions of maximum scalar dissipation rate, but these will not be shown in this paper to conserve space. Kerr (1985, figure 19) shows regions of strong scalar gradient with strong negative straining in his three-dimensional numerical simulation which are remarkably similar to those shown in figures 7 and 9 of the present paper.

Figure 10 shows conditioned averages of $(\nabla T)^2, |\nabla^2 T|$, and the ratio $|\nabla^2 T|/|\nabla|T|$, all as functions of the angle θ between the compressive strain axis and the scalar gradient, normalized by the maximum values of the functions. The angular range was divided into 5° bins, and the conditioned averages of the three quantities within each bin was computed for the eight realizations, giving $80 \times 80 \times 8 = 51\,200$ samples each. From figure 10 we see that large $\langle (\nabla T)^2 \rangle$ values are found when the alignment angle θ is nearly zero, but that $\langle |\nabla^2 T| \rangle$ hardly varies with θ at all.

The ratio $|\nabla^2 T|/|\nabla T|$ is the magnitude of the diffusion velocity of an isoscalar surface with respect to a fluid particle, except for the factor D

$$|u^T - u| = D\left(\frac{|\nabla^2 T|}{|\nabla T|}\right),$$

according to (3). As shown by the dotted line in figure 10, when the scalar gradient is aligned with the axis of compressive strain rate so that θ approaches zero, the average diffusion velocity is small compared with averages where θ is larger. This is a clear demonstration of the new strain-induced mixing mechanism, identified in this paper, which operates where the scalar gradients are high.

Also shown in figure 10 is the relative frequency of observation of samples as a function of the alignment angle θ (dot-dash line), which shows that the probability of gradient alignment is much higher than the probability of non-alignment. Curiously, the shape of this θ-histogram of sample values is almost identical to that of the θ-conditioned average $|\nabla T|^2$ shown by the solid line.

Another measure of the correlation between the strain-rate and scalar-gradient fields is the strain-magnitude–dissipation-magnitude correlation parameter

$$m \equiv \frac{\langle |\gamma| (\nabla T)^2 \rangle}{\langle |\gamma|^2 \rangle^{\frac{1}{2}} \langle (\nabla T)^2 \rangle} = \frac{\langle |\gamma| \chi \rangle}{\gamma_{\mathrm{rms}} \langle \chi \rangle},$$

which is found to be 0.78 ± 0.02 for the eight realizations discussed above. This parameter arises in the analysis of the next section.

In addition, the quantity

$$n \equiv \frac{\langle u_{,x'}^2 \rangle}{\langle |\gamma|^2 \rangle}$$

was computed since it provides a further indication of the alignment of the rate-of-strain axis with the scalar gradient, where x' is taken in the direction of the scalar gradient. For the eight realizations the average value of n was found to be 0.87 ± 0.03 compared with 1.0 if they were perfectly aligned everywhere and about 0.5 if they were uncorrelated. Kerr (1985, equations (44, 45)) computes fourth-order mixed scalar–velocity derivative correlations very similar to m and n for Pr values as small

as 0.1'. These correlations and their weighted sum are also large compared with uncorrelated values for $Pr < 1$, and show an increase with Re and possibly a tendency to converge to a constant value for various Pr values in Kerr (1985, figure 12).

6. Interpretation of Σ, m and $\langle \cos^2 \theta \rangle$ values

In this section we shall attempt to assess the relative importance of the two identified mixing mechanisms using the computed statistical parameters Σ, m and $\langle \cos^2 \theta \rangle$ of the numerical simulation.

Based on the definition of Σ in (1), Σ can be interpreted as a measurable version of the correlation coefficient for the alignment between ∇T and the rate-of-strain tensor $\boldsymbol{e}$, where $\boldsymbol{e}$ has components $e_{ij} = \frac{1}{2}(u_{i,j} + u_{j,i})$. We might expect a proportionality between $\Sigma \equiv \Sigma_{1D}$ and the more general quantity Σ_{3D}

$$\Sigma_{3D} \equiv \frac{\langle \nabla T \cdot \boldsymbol{e} \cdot \nabla T \rangle}{\langle \boldsymbol{e} : \boldsymbol{e} \rangle^{\frac{1}{2}} \langle \nabla T \cdot \nabla T \rangle}$$

$$= c_3 \Sigma_{1D}, \tag{8}$$

where c_3 is a universal proportionality constant.

Wyngaard (1971) gives the expression

$$\langle \nabla T \cdot \boldsymbol{e} \cdot \nabla T \rangle = \tfrac{15}{2} \langle u_{x,x} T_{,x}^2 \rangle \tag{9}$$

for three-dimensional isotropic turbulence. The terms in the denominator of (8) are

$$\langle \boldsymbol{e} : \boldsymbol{e} \rangle^{\frac{1}{2}} = [\tfrac{15}{2} \langle u_{x,x}^2 \rangle]^{\frac{1}{2}} \tag{10}$$

and

$$\langle \nabla T \cdot \nabla T \rangle = 3 \langle T_{,x}^2 \rangle, \tag{11}$$

also assuming isotropy. Combining (1), (8), (9), (10) and (11) gives

$$\Sigma_{3D} = (5/6)^{\frac{1}{2}} \Sigma_{1D} \tag{12}$$

so the universal constant c_3 is $(5.6)^{\frac{1}{2}} = 0.91$.

It can be shown (derivations of the isotropic (9) and (10) as well as (13) are given in the Appendix, for convenience) that the expression equivalent to (12) for the two-dimensional isotropic strain-rate–dissipation correlation coefficient Σ_{2D} is

$$\Sigma_{2D} = \Sigma_{1D}. \tag{13}$$

From (13) and the definition of Σ_{2D}

$$\Sigma_{1D} = \Sigma_{2D} = -\frac{\langle |\gamma| |\nabla T|^2 \cos 2\theta \rangle}{\langle 2|\gamma|^2 \rangle^{\frac{1}{2}} \langle |\nabla T|^2 \rangle}. \tag{14}$$

Now the numerator of the right-hand side of (14) has the form of a product average $\langle AM \rangle$ where $A \equiv \cos 2\theta$ is the alignment parameter and $M \equiv |\gamma| |\nabla T|^2$ is the magnitude product. The product average can be decomposed to determine if any correlation exists between the fluctuating components of A and M

$$\langle AM \rangle = \langle A \rangle \langle M \rangle + \langle A'M' \rangle, \tag{15}$$

where $\langle A' \rangle = \langle M' \rangle = 0$. From the previous discussion, the new large-gradient pinching mechanism 2 exists where both A and M are large, whereas the Gibson (1968a) zero-gradient pinching mechanism 1 is most effective where the alignment A is large but the magnitude product M is small. Therefore, any positive correlation
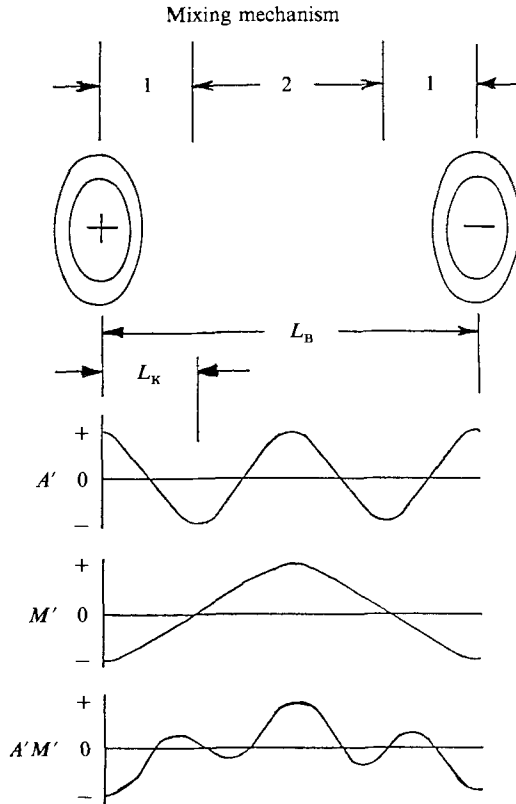
Mixing mechanism

FIGURE 11. Schematic distribution of A' and M' between adjacent hot and cold spots for $Pr < 1$. The 'hot-spot pinching' mechanism 1 should dominate within L_K of the extrema and cause $A'M'$ to be negative. The 'gradient-pinching' mechanism 2 should dominate elsewhere and cause $A'M'$ to be positive. The sign and magnitude of the average $\langle A'M' \rangle$ gives a measure of the relative importance of mechanism 1 versus mechanism 2.

between A' and M' can be attributed to mechanism 2 and any negative correlation to mechanism 1.

For $Pr > 1$, we might expect the effects of the two strain-mixing mechanisms to be indistinguishable from each other and from the Batchelor et al. (1959) wave crest compression mechanism because all of these are effective everywhere. However, for the present case with $Pr < 1$ we expect mechanism 1 to function within a distance of order L_K of an extremum (or a minimal-gradient surface) and mechanism 2 to be most effective halfway between extrema of opposite sign, where the gradients should be largest, as shown by the schematic diagram in figure 11. Since both mechanisms contribute to the product $\langle A \rangle \langle M \rangle$ in the same way, the two cannot be distinguished if the correlation $\langle A'M' \rangle = 0$, even when $Pr < 1$. Figure 11 shows the anticipated variation of A', M' and the product $A'M'$ in the regions between the hot spot and cold spot for $Pr < 1$, so that the two strain-mixing-mechanism regimes may be distinguished by the sign of the average $\langle A'M' \rangle$, as shown. If the sign is positive the implication is that mechanism 2 is the dominant strain-rate mechanism contributing to this component of the strain-rate parameter Σ. If it is negative then mechanism 1 is dominant.

Parameter	Value	Mechanism
Σ	-0.22 ± 0.01	1, 2
$\Sigma_{\text{alignment}}$	-0.154 ± 0.005	1, 2
$\Sigma_{\text{magnitude}}$	-0.066 ± 0.015	2
m	0.78 ± 0.02	1, 2
n	0.87 ± 0.03	1, 2
$\langle \cos^2 \theta \rangle$	0.64 ± 0.003	1, 2

TABLE 3. Strain-rate mixing parameters of the simulation

From (14), (15) and the definitions of m and M, so that $m = \langle M \rangle / \langle |\gamma|^2 \rangle^{\frac{1}{2}} \langle |\nabla T|^2 \rangle$, we find

$$
\begin{aligned}
\Sigma_{1D} &= \Sigma_{2D} \\
&= -\frac{\langle A \rangle m}{1.414} - \frac{\langle A'M' \rangle}{\langle 2|\gamma|^2 \rangle^{\frac{1}{2}} \langle |\nabla T|^2 \rangle} \\
&= \Sigma_{\text{alignment}} + \Sigma_{\text{magnitude}}.
\end{aligned}
\tag{16}
$$

Substituting $\Sigma = -0.22$, $\langle A \rangle = 2\langle \cos^2 \theta \rangle - 1 = 0.28$ and $m = 0.78$, from the last section, into (16) gives $\Sigma_{1D} = \Sigma_{2D} = -0.22$, $\Sigma_{\text{alignment}} = -0.154$ and $\Sigma_{\text{magnitude}} = -0.066$. Thus for the conditions of our simulation $\Sigma_{\text{magnitude}}$ is significantly non-zero and negative, and accounts for about 30% of the total strain–dissipation correlation coefficient Σ. Because $\langle A'M' \rangle$ is positive this component of Σ may be attributed to the new strain-mixing mechanism 2. The new mechanism can combine with other mechanisms such as the zero-gradient point and minimal-gradient surface stretching and pinching mechanism to produce the remaining 70%.

Table 3 summarizes the strain-rate-mixing parameters computed from the simulation. Each of the parameters gives evidence of strain-rate mixing, and each can be affected by either strain-mixing mechanism 1 or 2. The value of $\Sigma_{\text{magnitude}}$ shows that this parameter is dominated by mechanism 2.

7. One-dimensional numerical simulation of turbulent mixing for $Pr \ll 1$

As shown in figure 1 (*b*), mixing and diffusion for $Pr \ll 1$ depends on straining and diffusion along lines according to the Gibson (1968a) theory, suggesting that it may be useful to simulate these processes by one-dimensional modelling. Evidence of strong alignment of scalar gradients with rate-of-strain axes is given by the two-dimensional simulation above, and by the three-dimensional simulation of Kerr (1985) recently analysed by Ashurst *et al.* (1987). One-dimensional convection and diffusion are simulated along maximal- and minimal-gradient lines with lengths up to L_C. Rate-of-strain magnitudes are estimated using the universal turbulent velocity spectrum, assuming the Fourier components are in phase and compressing and stretching, respectively. Normalizing (2) with Kolmogorov length and time scales from table 2, the centred finite-difference expression for the scalar concentration C at time $t_K + \delta t_K$ is given by

$$
\begin{aligned}
C|_{t_K + \delta t_K} = C|_{t_K} + \left(\frac{\delta t_K}{(\delta x_K)^2 Pr} \right) [C|_{x_K + \delta x_K} + C|_{x_K - \delta x_K} - 2C|_{x_K}] \\
- \left(\frac{\delta t_K}{2\delta x_K} \right) u_K [C|_{x_K + \delta x_K} - C|_{x_K - \delta x_K}], \quad (17)
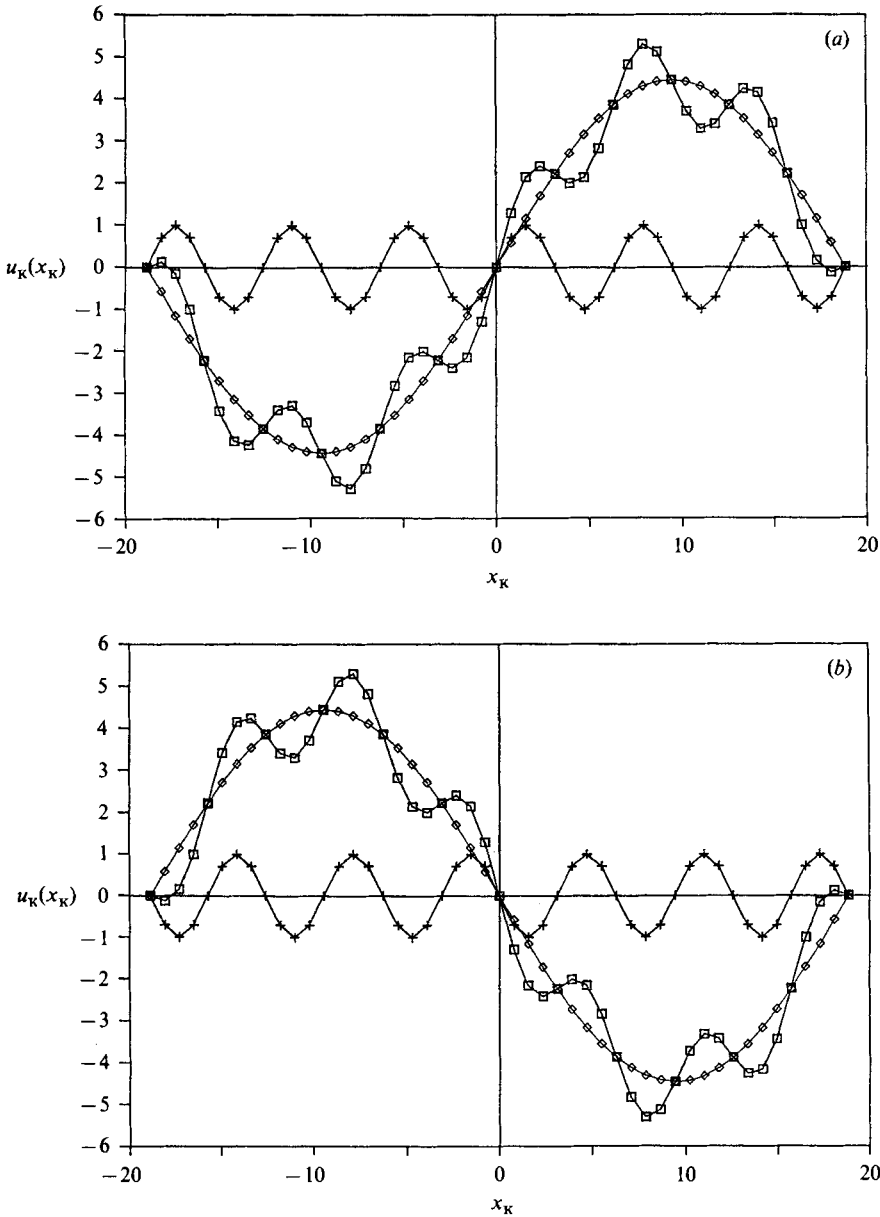\end{aligned}
$$

FIGURE 12 (*a,b*). For caption see facing page.

where $t_K = t\gamma$, $x_K = x/L_K$ and $u_K = u/(L_K\gamma)$. The first coefficient in parenthesis on the right side of (17) is set to $\frac{1}{2}$ for numerical stability, so the second coefficient in parenthesis on the right is $\frac{1}{4}\delta x_K Pr$. The velocity u for stretching in the x-direction is the sum of a sine wave with amplitude one and wavelength 2π plus a sine wave of amplitude $Pr^{-\frac{15}{24}}$ and wavelength $2\pi Pr^{-\frac{3}{4}}$ to simulate turbulence at a Reynolds number $Re = Re_{\mathrm{crit}}Pr^{-1}$ such that the energy scale $L_O = L_C = L_K Pr^{-\frac{3}{4}}$. For compression, the sign of u is reversed. The following simulations were carried out by the first author with a personal computer, using a commercial spreadsheet program to compute $C(t_K, x_K, Pr)$ from (17).
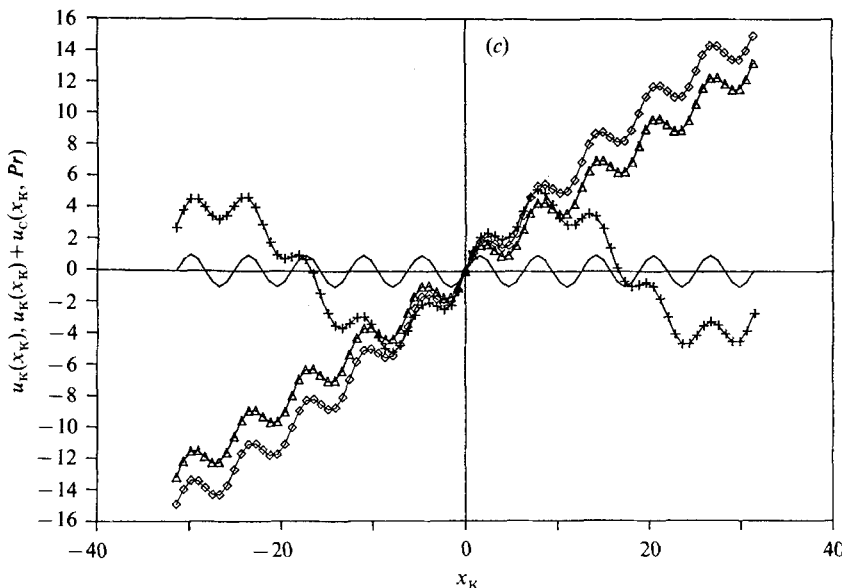
FIGURE 12. (a) Simulated turbulent velocity for diffusion stretching on a minimal-gradient line for turbulent mixing at $Pr = 0.1$ with $Re = Re_{\mathrm{crit}}Pr^{-1}$. The velocity is the sum ($\square$) of an L_{K} scale velocity ($+$) and an inphase velocity ($\Diamond$) at the energy scale L_{C}. (b) Same as (a) but for diffusion compression on a maximal-gradient line. (c) Same as (a) for $Pr = 0.1$ ($+$), 0.01 ($\Diamond$), and 0.001 ($\triangle$). The solid line shows the viscous scale velocity component.

Figure 12(a) shows the components and sum of the in-phase viscous and energy scale velocities for the simulated turbulent diffusion-stretch line for $Pr = 0.1$. Figure 12(b) is for a diffusion-compression line at the same Pr value. Figure 12(c) shows the stretch velocities for $Pr = 0.1$, 0.01 and 0.001. From figure 12(c) we see that the strain rate due to the energy scale velocity is comparable with that from the viscous scale velocity. The value near $x = 0$ is proportional to $Pr^{\frac{1}{6}}$ so, for the smallest Pr value of 0.001, the strain rate due to the energy scale is still 42% of that from the viscous scale, even though the lengthscales differ by a factor of 177.

Figure 13(a) shows the evolution of an extremum point with Gaussian initial distribution under the influence of the stretching velocity field of figure 12(a) for $Pr = 0.1$. The boundary condition at the largest scales, proportional to the Corrsin scale L_{C}, is insulation, with no flux in or out at $x = \pm 0.1^{-\frac{3}{4}}\pi L_{\mathrm{K}}$. For increasing time the extremum is stretched into a zero-gradient line as anticipated.

Figure 13(b) shows the evolution of the same initial concentration distribution as for figure 13(a), but under the compression velocity field of figure 12(b). The amplitude and radius of curvature of the extremum decrease rapidly with time, showing the rapid mixing which takes place when scalar gradients are increased by negative rates of strain.

Figure 13(c) compares the scalar distribution for the same initial and boundary conditions after the same time interval but for different velocity fields. The stretched and compressed distributions are the same as for figure 13(a, b). To see the effect of local strain, the velocity was set to one cycle of local compression for one Kolmogorov wavelength about the origin, with a 10% stretch outside this zone. The local compression distribution is almost identical to that for no velocity at all after the same time interval of $n = 60$. This shows that to be most effective in the low-Pr
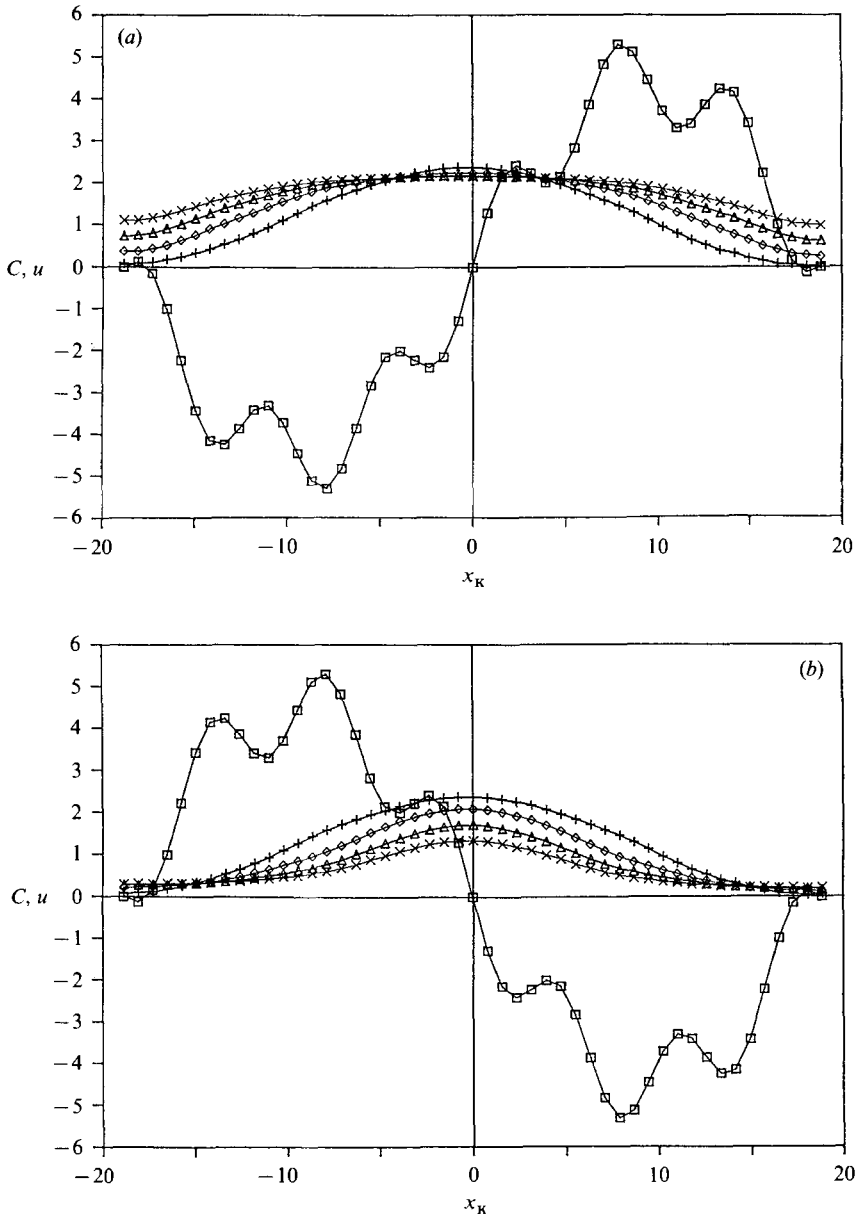
FIGURE 13 (a, b). For caption see facing page.

mixing process, the strain rate must be coherent over scales larger than L_K, which is consistent with one aspect of the central assumption of Batchelor *et al.* (1959). Thus, for γ to indeed be relevant to mixing for all Pr, it is necessary for any representative mixing model to show that straining can take place over lengthscales much larger than L_K with rates comparable with the local value γ in turbulent mixing with $Pr \ll 1$. The requirement is satisfied along diffusion-stretching and diffusion-compression lines, as shown in figure 12 (*a–c*) and in figure 16.

Figure 14 (*a*) shows the evolution of a ramp-like initial scalar distribution for $Pr = 0.001$ under the influence of the energy scale stretching for a simulated
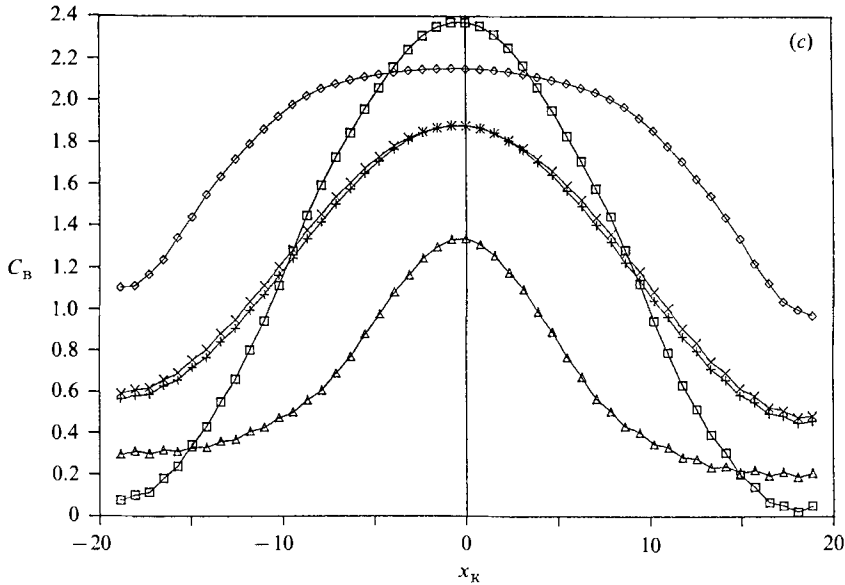
FIGURE 13. (a) Diffusion and convection for stretching along a minimal gradient line at $Pr = 0.1$. The velocity is shown by ($\square$), C for $n = 0$ ($+$), $n = 20$ ($\Diamond$), $n = 40$ ($\triangle$), ($n = 60$ ($\times$). The time interval is $\delta t_K = \frac{1}{2}(\delta x_K)^2 Pr$, and the time $t_K = n \delta t_K$. (b) Same as (a) but for compression along a maximal-gradient line. (c) Same as for (a) for different velocity fields at $n = 60$. Initial scalar distribution ($\square$), $u = 0$ ($+$), $u =$ stretching ($\Diamond$), $u =$ compression ($\triangle$), $u =$ local compression-far field stretching ($\times$).

$Re = Re_{crit} Pr^{-1}$ flow. The distribution rapidly flattens about the extremum point. This may be compared to the evolution of the same initial distribution with the sign of the velocity reversed to give compression, as shown in figure 14(b), where the distribution amplitude and lengthscale rapidly decrease. Clearly the stretched-out extrema of figures 14(a) and 12(a) will split into multiple extrema if slightly perturbed, for example by random lateral diffusion.

8. Summary and conclusions

A numerical simulation of low-Prandtl-number turbulent mixing is carried out in a homogeneous two-dimensional mixing field. From a comparison of the average zero crossing frequency of the scalar gradients and velocity gradients the effective Prandtl number is estimated to be about 0.1.

Examination of the computed strain-rate and scalar-gradient fields reveals that the strain rate produces mixing by two distinct mechanisms: (i) stretching, pinching, splitting and convection of zero-gradient points and minimal-gradient lines and surfaces, as prediced by Gibson (1968a); and (ii) strain–gradient alignment and amplification where the scalar gradients are particularly large in magnitude so that the isoscalar surfaces have a stronger than average tendency to be convected by the fluid motion. The second mixing mechanism is new, and may be explained using the expression

$$u^T = u - D(\nabla^2 T / |\nabla T|) g$$

for the velocity of an isoscalar surface, derived by Gibson (1968a).

An attempt is made in §6 to compare the effectiveness of the two mechanisms at
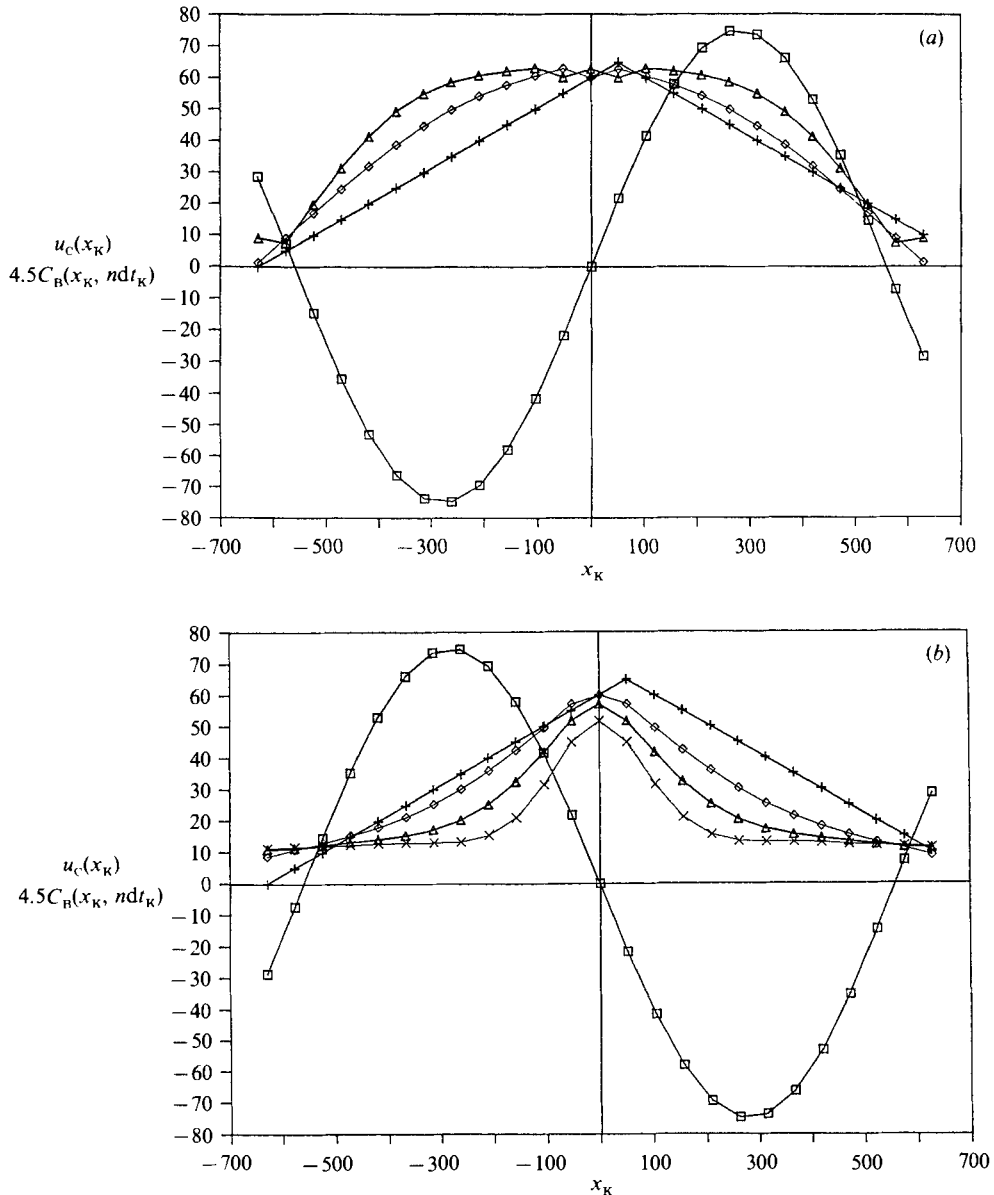
FIGURE 14. (a) Diffusion and convection for $Pr = 0.001$ with energy scale stretching. Velocity ($\square$), initial scalar distribution $n = 0$ ($+$), $n = 1$ ($\diamond$), $n = 2$ ($\triangle$). (b) Same as (a), but with L_{c} scale compression along a maximal-gradient line simulated.

producing strain-rate–dissipation correlation. According to this comparison, $\Sigma_{\mathrm{2D}} = -0.22$ is the sum of $\Sigma_{\mathrm{alignment}} = -0.15$ and $\Sigma_{\mathrm{magnitude}} = -0.07$. From the negative sign of the net $\Sigma_{\mathrm{magnitude}}$ we infer that this second component is dominated by mechanism 2. Mechanism 1 initiates the strain mixing by stretching out minimal-gradient surfaces, increasing the local gradients. These gradients are further amplified by the positive feedback of mechanism 2.

Both mechanisms contribute to an overall, Pr-independent, strain-mixing process which couples the rate-of-strain field to the scalar-dissipation field. This supports the

universal similarity hypothesis 1(a) of Gibson (1968b) in table 1, which states that small-scale structures of scalar fields should be universally similar for all Prandtl numbers when normalized with the Batchelor length, time, and scalar scales of table 2. Temperature spectra measured in mercury, air and water, with $Pr = 0.02$, 0.7 and 7, by Clay (1973), and recent numerical spectral estimates of Kerr (1986) for $Pr = 0.1$, 0.5 and 1, all collapse to approximately the same curve at high wavenumbers near L_B^{-1} under Batchelor scaling. These observations also support the Gibson (1968b) universal similarity hypothesis and contradict the proposal of Batchelor *et al.* (1959) and others that the local rate of strain should be irrelevant to mixing for $Pr < 1$.

The strain-rate–scalar-dissipation correlation coefficient Σ for the two-dimensional simulation was found to be about -0.22 compared to the experimental value of Clay (1973) of -0.4 and the recent three-dimensional numerical value of Kerr (1985) of -0.5. At this time it is not known why the two-dimensional value has a smaller magnitude. One possible explanation is that not all of the strain-rate-mixing processes have been simulated in two-dimensions. Vortex stretching may play an important role, although we note Kerr (1985) finds that $\langle \nabla T \cdot \omega \rangle$ decreases toward zero with increasing Reynolds number, where ω is the vorticity vector, indicating a tendency toward local two-dimensionality with scalar gradients perpendicular to the vorticity. Further studies of numerical mixing simulations with three-dimensional effects included and with wider variation of Prandtl number are needed to be sure that all important mixing processes have been identified, and to further assess their relative importance.

We conclude from the one-dimensional turbulent-scalar-mixing simulations of §7 that the local rate of strain is relevant to low-Pr turbulent mixing only if the rate of strain is correlated (of constant sign) over lengthscales very large compared with L_K, and with magnitudes comparable with local values γ. This is possible along maximal scalar gradient lines and minimal scalar gradient lines. Such lines will develop in turbulent scalar fields even for extremely small values of Pr if the Reynolds number of the flow is large enough to produce scalar extrema; that is, $Re \geqslant Re_{crit} Pr^{-1}$. The strain rates on such lines should be close to those of the local stretching and compression values, respectively. The line lengths will be of order L_C long compared with L_K, thus extending the range of influence of γ on the mixing process to scales larger than the maximum assumed by Batchelor *et al.* (1959).

The present study shows that numerical simulations of turbulent mixing processes may be used under circumstances that are difficult to reproduce experimentally. Despite the one- and two-dimensional nature of the simulations and other approximations to actual flows, the technique is clearly a valuable tool which will be increasingly used as its power and limitations are better understood and as computing capacity improves. Comparison of the present simulations with three-dimensional simulations such as Kerr (1985, 1986) is an obvious important next step.

Appendix

A.1. *Derivations of equations* (9) *and* (10)

Contractions of isotropic turbulence tensors expressed in terms of measurable quantities, such as (9) and (10), are usually presented without proof and tend to be treated as 'magic formulas' by students, and others. For convenience, we present the following derivations.

The general form of an isotropic tensor of rank 4 is given by the expression

$$D_{ijkl} = a\delta_{ij}\delta_{kl} + b(\delta_{ik}\delta_{jl} + \delta_{il}\delta_{jk}) + c(\delta_{ik}\delta_{jl} - \delta_{il}\delta_{jk}), \tag{A 1}$$

where a, b and c are scalars, as shown by Fung (1969, p. 193).

Consider the tensor of rank 4 formed from the scalar gradient and the rate-of-strain tensor

$$E_{ijkl} = T_{,i}\,e_{jk}\,T_{,l}. \tag{A 2}$$

Averaging (A 2) in a high-Péclet-number flow should give an isotropic tensor of rank 4 according to hypothesis 1 (a), table 1, so

$$\langle E_{ijkl} \rangle = \langle T_{,i}\,e_{jk}\,T_{,j} \rangle = a\delta_{ij}\delta_{kl} + b(\delta_{ik}\delta_{jl} + \delta_{il}\delta_{jk}) + c(\delta_{ik}\delta_{jl} - \delta_{il}\delta_{jk}) \tag{A 3}$$

from (A 1).

We can rewrite (A 3) in terms of scalars $p = b+c$ and $q = b-c$, which gives

$$\langle E_{ijkl} \rangle = a\delta_{ij}\delta_{kl} + p\delta_{ik}\delta_{jl} + q\delta_{il}\delta_{jk}. \tag{A 4}$$

For incompressible fluids, $e_{ij} = 0$, so setting $j = k$ in (A 4) gives

$$0 = a\delta_{ij}\delta_{jl} + p\delta_{ij}\delta_{jl} + q\delta_{il}\delta_{jj} = (a+p+3q)\,\delta_{il};$$

$$(a+p+3q) = 0,$$

where the quantity in parentheses must be zero since δ_{jl} is not. Repeated indices are summed over their range of values: $i, j, k, l = 1, 2, 3$ in three dimensions and $1, 2$ in two dimensions.

From the symmetry of the rate-of-strain tensor $e_{ij} = e_{ji}$ and (A 4)

$$\langle E_{ijkl} \rangle = \langle E_{ikjl} \rangle,$$

so from (A 4) $a\delta_{ij}\delta_{kl} + p\delta_{ik}\delta_{jl} + q\delta_{il}\delta_{jk} = a\delta_{ik}\delta_{jl} + p\delta_{ij}\delta_{kl} + q\delta_{il}\delta_{jk}$ (A 5)

giving $a = p$ (A 6)

by equating coefficients.

Combining (A 6) and (A 5) gives $a = -\frac{3}{2}q$, which is substituted in (A 4), along with (A 6), to give

$$\langle E_{ijkl} \rangle = a(\delta_{ij}\delta_{kl} + \delta_{ik}\delta_{jl} - \tfrac{2}{3}\delta_{il}\delta_{jk}). \tag{A 7}$$

Setting $i = j = k = l = 1$ in (A 7)

$$\langle E_{1111} \rangle = a(\delta_{11}\delta_{11} + \delta_{11}\delta_{11} - \tfrac{2}{3}\delta_{11}\delta_{11}) = \tfrac{4}{3}a. \tag{A 8}$$

From (A 7) and (A 8) we see that

$$\langle E_{ijkl} \rangle = \tfrac{3}{4}\langle E_{1111} \rangle\,(\delta_{ij}\delta_{kl} + \delta_{ik}\delta_{jl} - \tfrac{2}{3}\delta_{il}\delta_{jk}) \tag{A 9}$$

which is the general expression for the isotropic tensor in three dimensions.

Setting $i = j$ and $k = l$ in (A 9) gives

$$\langle E_{iikk} \rangle = \tfrac{3}{4}\langle E_{1111} \rangle (\delta_{ii}\,\delta_{kk} + \delta_{ik}\,\delta_{ik} - \tfrac{2}{3}\delta_{ik}\,\delta_{ik})$$
$$= \tfrac{3}{4}\langle E_{1111} \rangle (3 \times 3 + 3 - 2) = \tfrac{15}{2}\langle E_{1111} \rangle$$

which verifies equation (9) quoted by Wyngaard (1971).

Equation (10) may be similarly obtained.

A.2. *Derivation of equation* (13)

We now derive the relation $\Sigma_{2D} = \Sigma_{1D} = \Sigma$ between the strain–dissipation correlation coefficients for two-dimensional isotropic flow and the one-dimensional measurable quantity Σ given by (1).

The form of the two-dimensional isotropic tensor of rank 4 is identical to (A 4),

$$\langle E_{ijkl} \rangle = a\delta_{ij}\,\delta_{kl} + p\delta_{ik}\,\delta_{jl} + q\delta_{il}\,\delta_{jk}, \tag{A 10}$$

except that the indices i, j, k, l now have values $(1, 2)$ rather than $(1, 2, 3)$. For an incompressible fluid, (A 10) becomes zero when $j = k$, which for two-dimensional flow gives $a + p + 2q = 0$ because $\delta_{jj} = 2$.

The symmetry condition gives $a = p$ so $a = -q$, both of which are substituted in (A 10):

$$\langle E_{ijkl} \rangle = a(\delta_{ij}\,\delta_{kl} + \delta_{ik}\,\delta_{jl} - \delta_{il}\,\delta_{jk}) \tag{A 11}$$

to give the general expression for the isotropic tensor in two-dimensions.

We can interpret the scalar a by setting $i = j = k = l = 1$ in (A 11)

$$\langle E_{1111} \rangle = a(\delta_{11}\,\delta_{11} + \delta_{11}\,\delta_{11} - \delta_{11}\,\delta_{11}) = a \tag{A 12}$$

so that the general expression is

$$\langle E_{ijkl} \rangle = \langle E_{1111} \rangle (\delta_{ij}\,\delta_{kl} + \delta_{ik}\,\delta_{jl} - \delta_{il}\,\delta_{jk}) \tag{A 13}$$

for the isotropic tensor in two-dimensions, which may be compared to the three-dimensional expression (A 9).

Setting $i = j$ and $k = l$ in (A 13) gives

$$\langle E_{iikk} \rangle = \langle E_{1111} \rangle (\delta_{ii}\,\delta_{kk} + \delta_{ik}\,\delta_{ik} - \delta_{ik}\,\delta_{ik})$$
$$= \langle E_{1111} \rangle (2 \times 2 + 2 - 2) = 4\langle E_{1111} \rangle \tag{A 14}$$

with coefficient 4 for this two-dimensional expression rather than $\tfrac{15}{2}$ for the three-dimensional expression given by (9).

Substituting (A 14) and the equivalent expression $\langle e\!:\!e \rangle = 4\langle u_{x,x}^2 \rangle$ into the definition of Σ_{2D} gives

$$\Sigma_{2D} = \langle E_{iikk} \rangle / \langle e\!:\!e \rangle^{\frac{1}{2}} \langle \nabla T \cdot \nabla T \rangle$$
$$= 4\langle E_{1111} \rangle / \langle 4u_{x,x}^2 \rangle^{\frac{1}{2}} \langle 2T_{,x}^2 \rangle$$
$$= \Sigma_{1D}$$

which is equation (13) that we wanted to prove.

REFERENCES

ASHURST, W. T. 1979 Numerical simulation of turbulent mixing layers via vortex dynamics. In *Turbulent shear flows I* (ed. F. Durst, B. E. Launder, F. W. Schmidt & J. H. Whitelaw), pp. 402–443. Springer.

ASHURST, W. T. & BARR, P. K. 1983 Stochastic calculation of laminar wrinkled flame propagation via vortex dynamics. *Combust. Sci. Tech.* **34**, 227.

ASHURST, W. T., KERSTEIN, A. R., KERR, R. M. & GIBSON, C. H. 1987 Alignment of vorticity and scalar gradients with strain rate in simulated Navier–Stokes turbulence. *Phys. Fluids* **30**, 2343–2353.

BATCHELOR, G. K. 1959 Small-scale variation of convected quantities like temperature in turbulent fluid. Part 1. General discussion and the case of small conductivity. *J. Fluid Mech.* **5**, 113–133.

BATCHELOR, G. K., HOWELLS, I. D. & TOWNSEND, A. A. 1959 Small-scale variation of convected quantities like temperature in turbulent fluid. Part 2. The case of large conductivity. *J. Fluid Mech.* **5**, 134–139.

BOSTON, N. E. 1970 An investigation of high wave number temperature and velocity spectra in air. Ph.D. thesis, University of British Columbia.

CLAY, J. P. 1973 Turbulent mixing of temperature in water, air and mercury. Ph.D. thesis, University of California at San Diego.

CORRSIN, S. 1951 On the spectrum of isotropic temperature fluctuations in isotropic turbulence. *J. Appl. Phys.* **22**, 469–473.

FUNG, Y. C. 1969 *First-Course in Continuum Mechanics*, 2nd edn. Prentice Hall.

GIBSON, C. H. 1968*a* Fine structure of scalar fields mixed by turbulence, I. Zero gradient points and minimal gradient surfaces. *Phys. Fluids* **11**, 2305–2315.

GIBSON, C. H. 1968*b* Fine structure of scalar fields mixed by turbulence, II. Spectral theory. *Phys. Fluids* **11**, 2316–2327.

GIBSON, C. H. & KERR, R. M. 1988 Evidence of turbulent mixing by the rate-of-strain. *Invited lecture by C.H.G. for the Tenth Turbulence Symp., University of Missouri-Rolla, September 21–23, 1986 (conference preprint). Phys. Fluids* (submitted).

GIBSON, C. H. & SCHWARZ, W. H. 1963 The universal equilibrium spectra of turbulent velocity and scalar fields. *J. Fluid Mech.* **6**, 365–386.

GOLITSYN, G. S. 1960 Fluctuations of the magnetic field and current density in a turbulent flow of a weakly conducting fluid. *Dokl. Akad. Nauk SSSR* **32**, 315.

GRANATSTEIN, V. L., BUCHSBAUM, S. J. & BUGNOLO, D. S. 1966 Fluctuation spectrum of a plasma additive in a turbulent gas. *Phys. Rev. Lett.* **6**, 504.

HILL, R. J. 1978 Models of the scalar spectrum for turbulent advection. *J. Fluid Mech.* **88**, 541–562.

KERR, R. M. 1985 Higher-order derivative correlations and the alignment of small-scale structures in isotropic numerical turbulence. *J. Fluid Mech.* **153**, 31–58.

KERR, R. M. 1986 Kolmogoroff and scalar spectral regimes in numerical turbulence. *NASA Tech. Mem.* in preparation.

KERSTEIN, A. R. & ASHURST, W. T. 1984 Lognormality of gradients of diffusive scalars in homogeneous, two-dimensional mixing systems. *Phys. Fluids* **27**, 289.

KOLMOGOROV, A. N. 1941 The local structure of turbulence in incompressible viscous fluid for very large Reynolds number. *Dokl. Akad. Nauk SSSR* **30**, 301.

KOLMOGOROV, A. N. 1962 A refinement of previous hypotheses concerning the local structure of turbulence in a viscous incompressible fluid at high Reynolds number. *J. Fluid Mech.* **3**, 82–85.

KRAICHNAN, R. H. & NAGARAJAN, S. 1967 Growth of turbulent magnetic fields. *Phys. Fluids* **10**, 859.

LARCHEVEQUE, M., CHOLLET, J. P., HERRING, J. R., LESIEUR, M., NEWMAN, G. R. & SCHERTZER, D. 1980 Two-point closure applied to a passive scalar in decaying passive turbulence. In *Turbulent Shear Flows II* (ed. J. S. Bradbury, F. Durst, B. E. Launder, F. W. Schmidt & J. H. Whitelaw), pp. 50–60. Springer.

MOFFATT, H. K. 1961 The amplification of a weakly magnetic field by turbulence in fluids of moderate conductivity. *J. Fluid Mech.* **11**, 625–635.

MOFFATT, H. K. 1962 Intensification of the earth's magnetic field by turbulence in the atmosphere. *J. Geophys. Res.* **67**, 307.

OBUKHOV, A. M. 1949 Struktura temperaturnovo polia v turbulentnom potoke. *Izv. Akad. Nauk SSSR Ser. Geofiz.* **3**, 59.

WYNGAARD, J. C. 1971 The effect of velocity sensitivity on temperature derivative statistics. *J. Fluid Mech.* **48**, 763–769.